SSEC No.71.09.S1

ANNUAL REPORT—1970: STUDIES OF THE ATMOSPHERE USING AEROSPACE PROBINGS

SPACE SCIENCE AND ENGINEERING CENTER, THE UNIVERSITY OF WISCONSIN

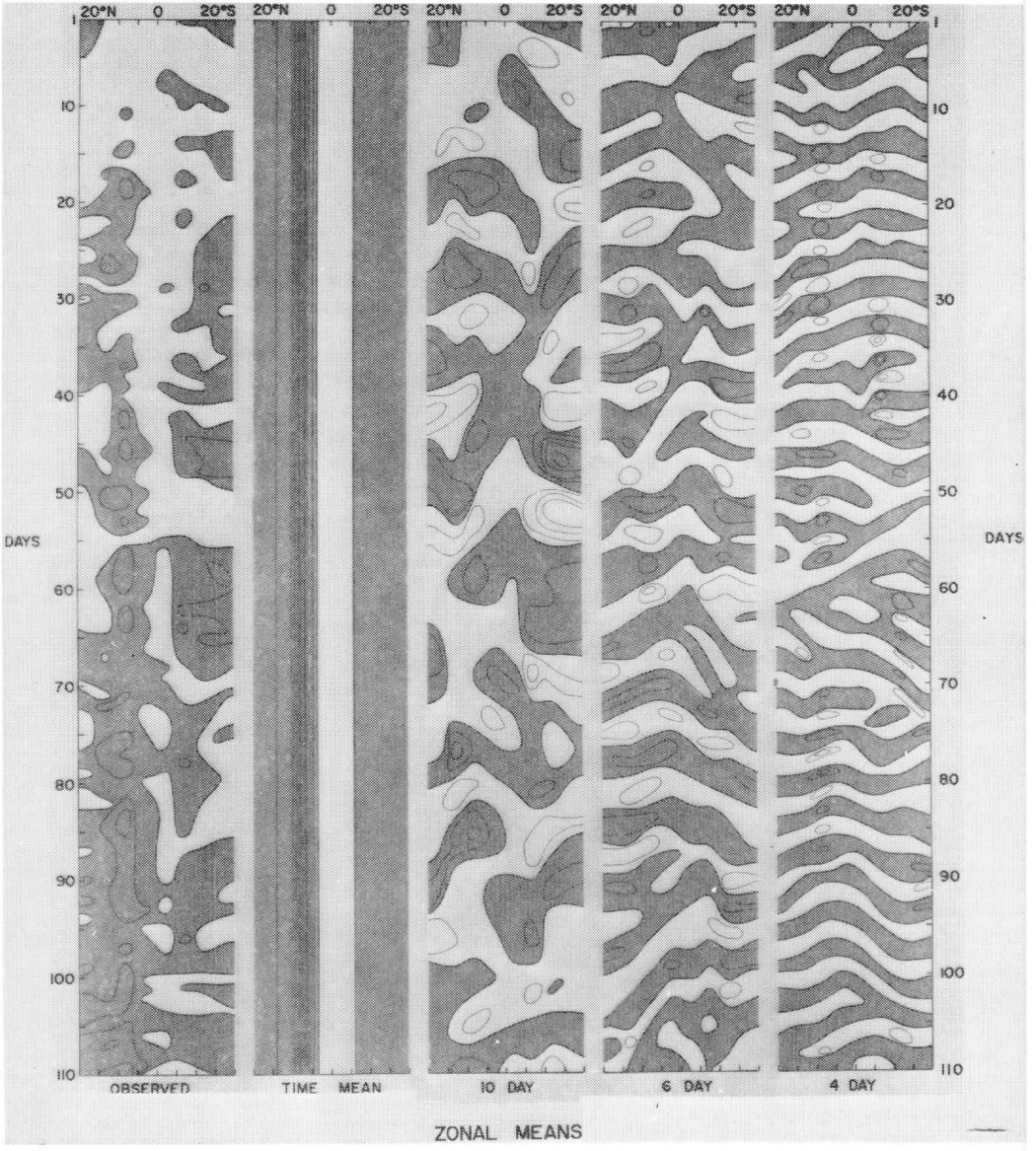

Cover Photograph

The photograph depicts the zonal means of cloud cover in the tropical Pacific during the summer of 1967. The shaded regions in the observed and in the time mean represent 20% or more cloud cover while for ten-, six- and four-day period filtered data they are the regions of positive anomaly.

This picture, in general, reflects planetary scale cloud activity in the tropical Pacific. The latitude-time structure of these fluctuations indicates the various modes of coupling between different latitudes for each frequency band. This information is a natural extension of the spectral study of cloud amount presented in this report.

Space Science and Engineering Center,
The University of Wisconsin
Madison, Wisconsin

STUDIES OF THE ATMOSPHERE USING AEROSPACE PROBINGS

Annual Report on

ESSA Grant E-230-G

1970

The research reported in this document has been supported by the National Oceanic and Atmospheric Administration.

September 1971

PRINCIPAL INVESTIGATOR

Verner E. Suomi

CONTRIBUTIONS BY

Sikdar, D. N.
Suchman, D.
Suomi, V. E.
Young, J. A.
Young, J. T.

PREFACE

The research documented in this report consists of continuing studies on tropical meteorology both from observational and theoretical viewpoints. The first paper in this series is an example how time-lapse images can be useful for extracting statistical information on tropical "easterly" and planetary waves. The future application of geosynchronous satellite data for such explorations in tropical circulations hardly needs emphasis.

The second paper deals with some of the theoretical aspects related to low-level convection often observed from a geostationary altitude. Lastly, a paper is included that describes a technique to rectify and grid ATS satellite pictures in real time based on geographic features in the picture. The product has high utility and is quite versatile.

During this report period outstanding progress has been made in developing software to determine cloud motion vector with high precision ($\pm$ 2 knots, $\pm$ 10°). Our next report will include a progress report in this area.

It is a pleasure for me to acknowledge the many contributions of my associates. They are the individuals who make this report possible.

Verner E. Suomi
Principal Investigator

CONTENTS

Time-Spectral Characteristics of Large-Scale Cloud Systems in the Tropical Pacific

by
D. N. Sikdar, J. A. Young and V. E. Suomi
The University of Wisconsin, Madison

Abstract

Time series of areal cloud coverage over the Central Pacific are studied to determine the large-scale variations of tropical disturbance activity for a four-month period in 1967. The persistent and fluctuating components are found to be more prevalent in the Northern Hemisphere and Southern Hemisphere, respectively, with major variations in activity evident between the eastern and western parts of the Southern Hemispheric portion. Normalized power spectra show that the transient activity occurring in the equatorial zone is dominated by the shorter periods of about four days, while longer periods are dominant away from the equator. Coherency magnitudes and phases between different locations indicate that propagating cloud systems are most identifiable at the lower frequencies and in the Southern Hemisphere. Wavelength estimates are uncertain for the shorter periods, but activity with periods in excess of five days consists largely of westward propagation on the planetary wave scale.

1. Introduction

The existence of moving systems of cloudiness and rainfall has long been of interest to the tropical meteorologist, and the development of the easterly wave model (Riehl, 1945) provided an idealization which was useful for the practitioner. At the same time, it was recognized that important geographical variations in the extent and type of disturbance behavior left much to be learned. For example, Palmer (1951) identified several different subregions of the Central Pacific whose "disturbance climatologies" differed.

These classifications seem to be in remarkable agreement with recent studies of satellite cloud data, particularly those of Kornfield, et al. (1967), Hubert, et al. (1969), and Chang (1970).

The advent of the ATS geostationary satellite has, in addition to providing more complete coverage of the tropics, stimulated new efforts to study conventional wind observations in an attempt to understand the dynamics of the disturbances. The main technique used in these studies has been that of time-series analysis. While many different conclusions have been reached in these investigations, the existence of wind field fluctuations with periods of the order of four to five days is well documented (Rosenthal, 1960; Yanai, et al., 1968; Wallace and Chang, 1969; Nitta, 1970(a)). Sikdar and Suomi (1970) noted similar periods in the cloud systems which they defined to be convectively active, while Chang (1970) noted a predominance of four-day periods in his study of time-composite photographs of total cloud activity.

It is tempting to associate these fluctuations with the classical easterly wave disturbances which were considered to have longitudinal wavelengths on the order of 2,500 km. However, the statistical estimates of wavelengths taken from the time-series studies present a confused picture, possibly due to the irregular array of reporting stations in the tropics. Many estimates are in the range of 2,000 km. - 5,000 km. (Wallace and Chang, 1969; Chang, 1970; Nitta, 1970(a)), but both Yanai, et al. (1968), and, in the eastern Pacific, Nitta (1970(a)) estimate wavelengths of 10,000 km.

Wind field fluctuations are by no means limited to these relatively short-lived motions. In fact, the spectral studies indicated large amounts of activity with significantly longer time scales. Evidence of a minor spectral peak at seven days was given by Yanai and Murakami (1970) and Nitta (1970(b)), while periods longer than ten days and presumably associated with planetary wave activity were noted by Wallace and Chang (1969), Yanai and Maruyama (1966), and Nitta (1970(b)).

Consideration of yet longer periods takes one into the realm of seasonal or even inter-annual variations. Wallace and Chang (1969) took special note of such slow changes in the intensity of waves with four-day periods; it is thought that they may account for some of the differences between the conclusions drawn in the various studies discussed above. In addition, Hubert, et al. (1969) have noted year-to-year differences in the weak ITCZ of the southeastern Pacific.

For the most part the analysis of cloud data has been less quantitative than the wind analyses. The present study is an attempt to extend the spectral results to include satellite cloud data. More importantly,

this study is not limited to particular locations, but allows a complete geographical coverage of the Central Pacific area. As a result, an extensive "climatology" of large-scale variations in persistence, spatial scale and intensity may be quantitatively deduced which supplements the conclusions of Chang (1970). To accomplish this task, subsequent sections deal with the distribution of persistent and transient cloud activity over a large portion of the Pacific Ocean. Patterns of normalized spectra are presented, and cross-spectra are utilized to characterize disturbance lifetimes and scales.

2. Basic Cloud Data

We have chosen the Pacific Ocean for this study in order to minimize the obscuration of the traveling disturbances by continental effects. To facilitate comparison of the present results with those of previous studies, portions of both the eastern and western Pacific are included. The large-scale geographical differences in temporal behavior are resolved by a regular array of rectangular sectors in latitudinal belts 10° wide and 20° in longitudinal breadth, as shown in Figure 1. The locations of most wind studies have been mainly limited to portions of sectors N2-N5 and N7-N10 so that the present coverage represents an improvement. The size of the sectors allows the largest spatial variations to be analyzed, including the geographical changes in the traveling "cloud cluster" systems. However, the actual resolution of their detailed structure is not possible with this grid.

The basic cloud data was obtained from daily ESSA-III mosaics for the period April 1–July 31, 1967 and is shown in composite time series form in Figures 2 and 3. This period includes much of the Northern Hemisphere's wet season and part of the dry season in the Southern Hemisphere, especially at locations further than 10° from the equator. The figures seem to emphasize the complex picture of traveling cloud patterns such that relatively slight geographical separations yield significant differences in the amount of cloud, its persistence, and dominant scale. There is some evidence that the traveling wave regimes which are not obscured by persistent patterns exhibit a certain intermittency in their activity. These patterns are more complicated than those presented by Chang (1970) for a more limited length of time and latitudinal extent. In fact, while Chang noted a predominance of westward propagation, the figures here also indicate occasional regimes of apparent eastward movement.

It is clear that meaningful conclusions from this data are aided by a complete statistical analysis. To reach this end, the cloud distributions in Figures 2 and 3 were converted to time-series of daily values of planimetered areal cloud amounts for each of the twenty sectors.

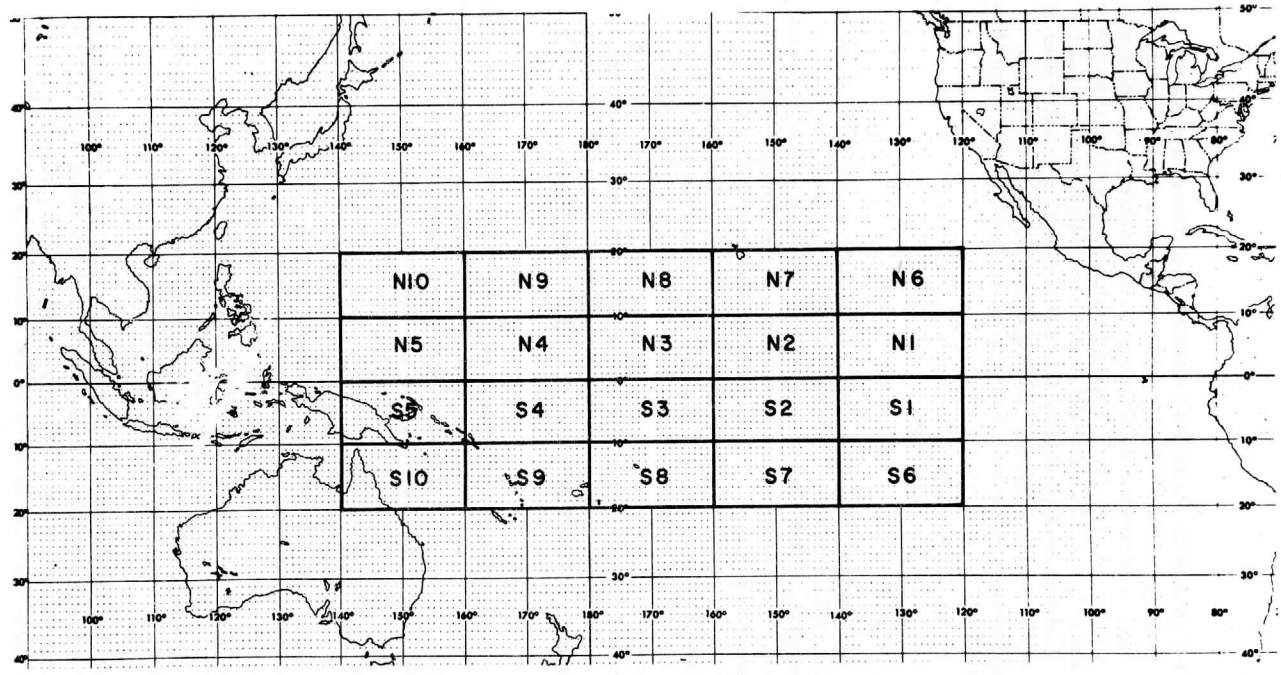

Figure 1. Study area over the Central Pacific Ocean

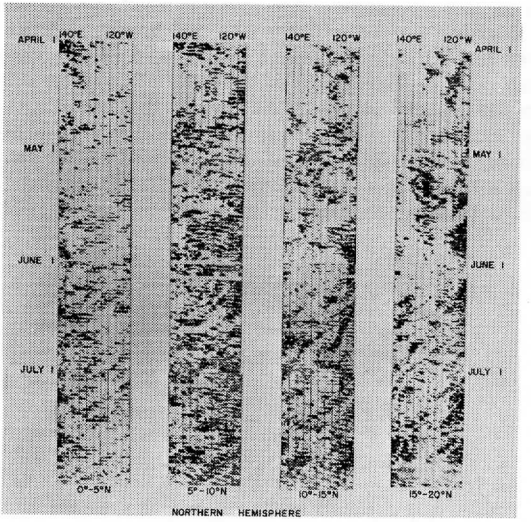

Figure 2. Longitude-time sections of Northern Hemispheric cloud distributions (shaded) for 5° latitudinal belts taken from ESSA III mosaics. Brighter cloud regions are darkened. Meridians are indicated at 10° intervals.

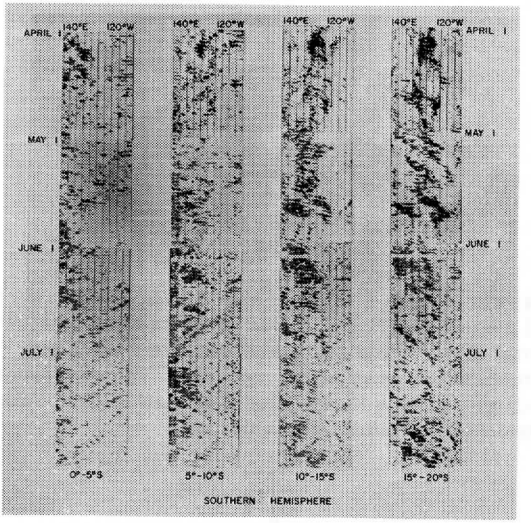

Figure 3. Same as Figure 2, except for Southern Hemisphere

The top portions of Figure 4 show that the mean cloud amounts range from about 10% to 30% coverage. Two axes of maximum amount are apparent. One lies near the latitudinal belt 0° - 10° N which is the location of the ITCZ as seen in both rainfall (Riehl, 1954) and mean cloudiness patterns (Kornfield, et al., 1969; Hubert, et al., (1969). The latter authors, using data taken from the same time period as this study, noted that a similar structure in the Southern Hemisphere is missing, since a well-marked "dry zone" exists in sectors S1-S3. This zone is terminated at its western end by a pronounced band of mean cloudiness and rainfall which extends along an axis from S5 to S8. Interestingly, the minimum in sector N7 coincides

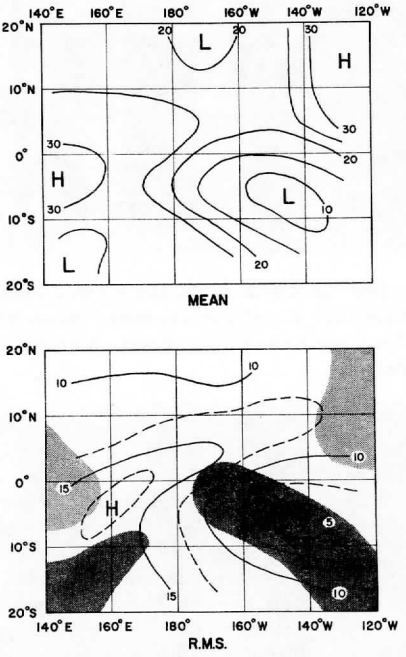

Figure 4. Gross cloud-area statistics over Pacific study area for period April 1—July 31, 1967. Cloud amounts are expressed in percent of total area. Solid isoline interval is 5%. Heavy (light) shading represents areas where root-mean-square amounts are larger (smaller) than 0.6 (0.4) times the mean amount. Latitudinal scale is exaggerated by a factor of 2.

with the area where Chang (1970) noticed that the disturbances weakened as they progressed westward during this same time period.

The root-mean-square amounts, which reflect the intensity of transient activity, are seen to range from 5% to 18%. This range is less than the range of mean amounts but still represents a variance range of one order of magnitude. The main axes of transient activity closely follow those of the mean patterns, suggesting that the mean amounts are produced largely by traveling disturbances. The significance of this value is that it represents the relative variability of a simple sinusoidal variation of cloudiness with a minimum value of zero. For sinusoidal variations with smaller values of relative variability, the minimum cloudiness amount is not zero, indicating a persistent component. The patterns in the Northern Hemisphere's ITCZ region are more persistent than in the Southern Hemisphere, where, for example, the dry-zone cloudiness is associated mainly with transient disturbances.

3. Spectral Results

In order to examine the time variation more closely, the time series (122 days in length) were next subjected to a high-pass filter and then spectrally analyzed. The filtering was accomplished by following Maruyama (1968) and applying a twenty-three-point normalized Gaussian weighting function with standard deviation of 5.0 days to the data. The effect of this filter was to severely attenuate power for periods in excess of twenty days, leaving shorter periods nearly intact. Using a lag of fifteen days, sixteen smoothed spectral estimates (at intervals of .033 c.p.d.) were obtained following the techniques outlined in Panofsky and Brier (1965). With thirteen equivalent degrees of freedom, the probability is 80% that the true spectral density is within approximately $\pm$ 50% of the spectral estimate calculated here. The estimated quantities included power spectra of a single series and cross-spectra of two separate series. The large spatial differences in total variance dominated the power spectra; to alleviate this effect the power spectra were then normalized, allowing one to focus upon the relative contributions of a given frequency band to the total variance.

Figures 5 and 6 show the normalized filtered power spectra of cloud amounts for each of the twenty sectors. The attenuation of low-frequency power by the filtering procedure is evident in each spectrum. The normalization procedure has forced the total areas under each curve to be identical, thus emphasizing the differences in spectral shapes, which are seen to be considerable. Inspection of the curves shows quickly that the lower frequencies tend to dominate the higher ones, but in a manner which seems to contain a variety of realizations which depend upon both latitude and longitude. The relative lack of power at the highest frequencies seems to

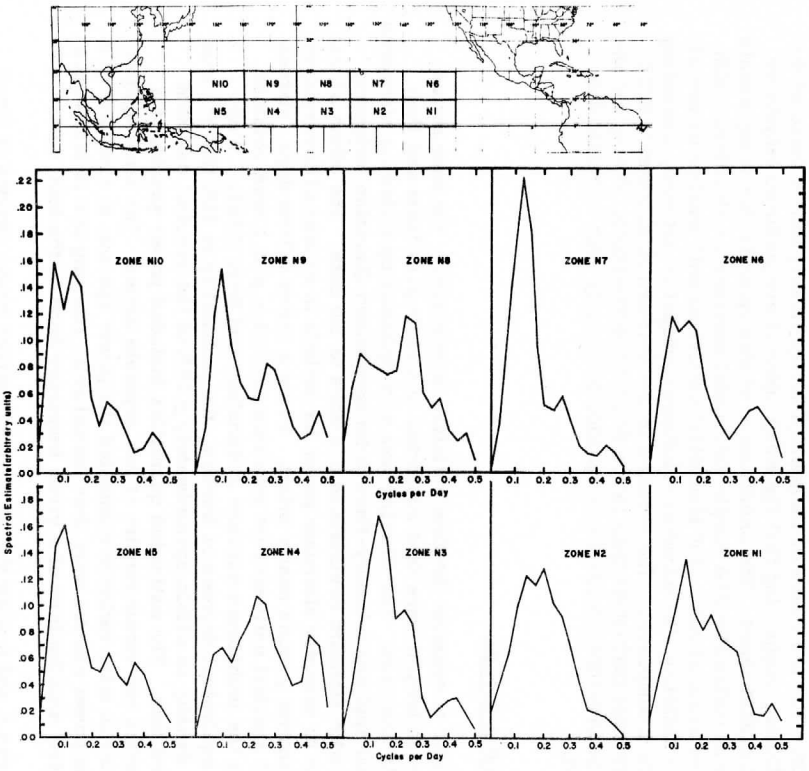

Figure 5. Normalized power spectra of areal cloud amount in each of ten Northern Hemispheric sectors, obtained from series with power at frequencies less than . 05 c. p. d. attenuated by filtering.

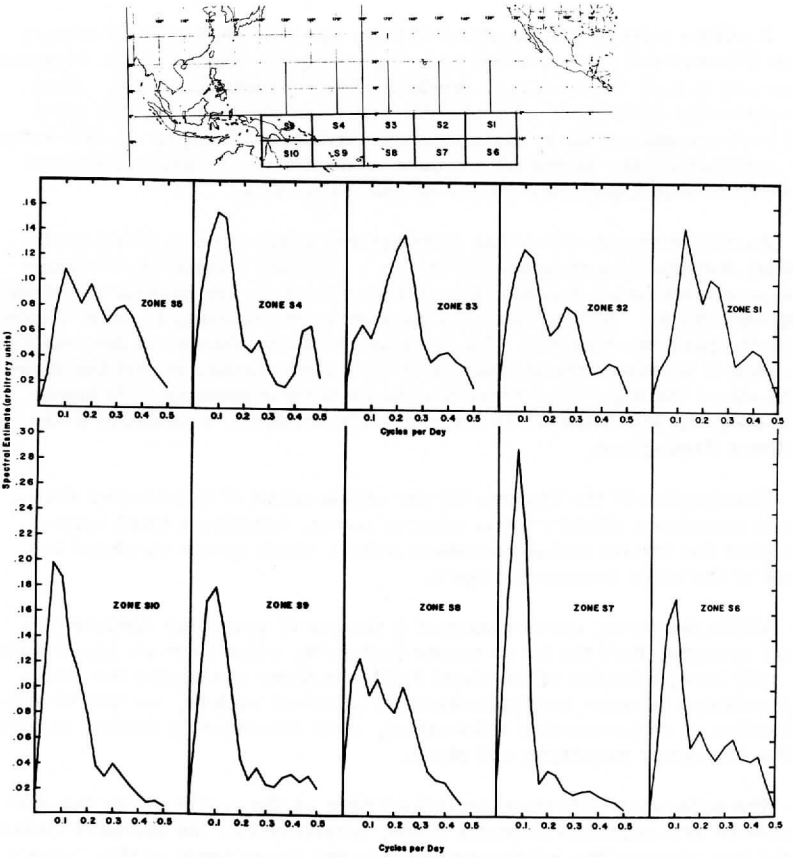

Figure 6. Same as Figure 5, except for Southern Hemisphere

guarantee these estimates to be free of aliasing about the Nyquist frequency of 0.5 c.p.d.

A simple tally of the locations of local spectral peaks for all sectors quickly brings out the existence of a dominant peak located in the frequency range .08 c.p.d. – .12 c.p.d. (periods of nine to thirteen days). There are also good indications of a secondary peak at about four to five days, and even a tendency for a slight maximum at about 2.5 days. In this sense, the spectrum for the sector S2 seems to characterize the main qualitative features of that appropriate for the domain as a whole.

An easier comparison of the geographical differences is found in the spatial distributions presented in Figure 7. Spatial variations in normalized power are large, ranging by a factor of three for the highest and lowest frequency bands. A remarkably simple inverse relationship is seen to exist between these two patterns. For example, sectors adjacent to the equator are seen to be relatively inactive in the low frequencies, at just the locations where the high frequencies tend to be at their maximum. At higher latitudes, the low frequencies are relatively dominant, especially in the Southern Hemisphere.

Examination of the diagram for the middle range of frequencies shows that it contains a slightly lower level of power, exhibits a small variation over the domain and possesses a pattern which seems unrelated to those of the other frequency ranges.

While the power spectra suggest a variety of wave-like motions of cloud systems, they are by no means definitive, since they are based upon the only local behavior of the cloud field. In order to examine the interrelationships between the fluctuations in different sectors, we turn to consideration of cross-spectral information, most conveniently defined in terms of the coherency magnitude and phase.

The coherency magnitude is defined here as the length of the "vector" in the co- and quadrature-spectra plane, normalized by the geometric mean of the two spectra; the coherency phase is the phase angle of this "vector." Basically, the coherency magnitude may be thought of as a correlation magnitude between two time series whose power is restricted to the same frequency band. In the present application, it indicates the existence of identifiable linear relationships between the cloud fluctuations in adjacent sectors (N2-N1, N3-N2, ...) lying in the same latitude range. For moving wave-like patterns, a large coherency reflects a relatively long lifetime for the system, while small coherencies reflect a short lifetime or an ill-defined wavelength at that period. Since coherency estimates for very narrow frequency bands necessarily approach the maximum magnitude of 1.00, their information content is optimized when frequency bands of intermediate width are considered. The coherency estimates discussed below

have accordingly been obtained by vector averaging the original narrow-band estimates; this has the effect of reducing the magnitudes when the phases are scattered, while consistent phase relationships produce a final magnitude which is nearly the average of the individual magnitudes.

The cloud-cover coherency magnitudes are presented in Figure 8. In each frequency range the patterns seem well-defined, but they do not appear to relate simply to the spectral levels presented in Figure 7 except possibly at low frequencies, where the regions of strong activity also seem to be geographically coherent. Coherency magnitudes are also relatively large in the middle frequency band, especially in the Southern Hemisphere

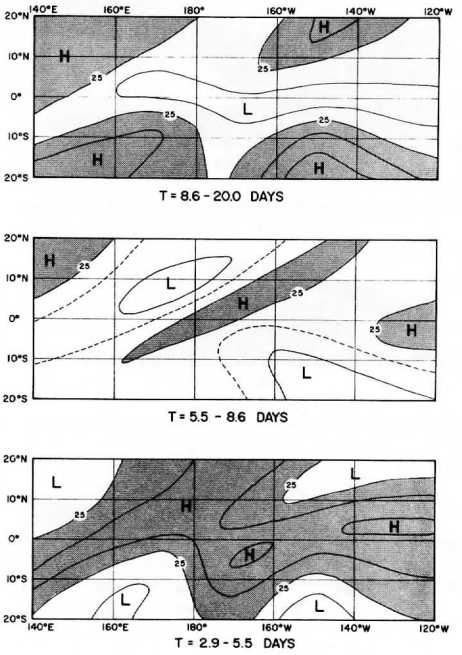

Figure 7. Spatial distribution of normalized power spectral amounts of cloud-cover for separate frequency bands. Units for each band are percent of total variance in all periods less than twenty days. Solid isoline interval is 10%.

away from the "dry zone" in the eastern portion. Generally, the high-frequency patterns appear relatively incoherent, indicating that the patterns grow, decay, or shift their wavelength significantly over the 20° longitudinal width of the sectors. Curiously, the largest coherence for these systems is found near the "dry zone" region of incoherent long-period activity.

The interpretation of these estimates in terms of simple wave propagation depends upon the distribution of coherency phases. The phases shown in Figure 9 are taken from coherencies involving each sector with sector S4;

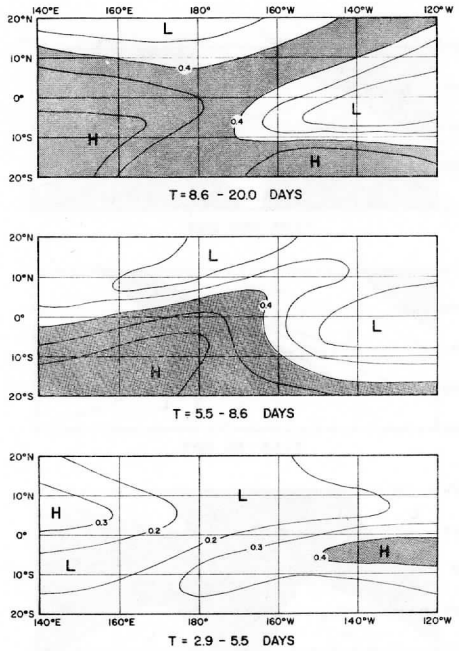

Figure 8. Spatial distribution of local cloud-cover coherency magnitude for separate frequency bands. Magnitude at each point is determined from mean "vector" coherencies involving the two adjacent sectors at the same latitude. Shading denotes values in excess of 0.4. Isoline interval is 0.1.

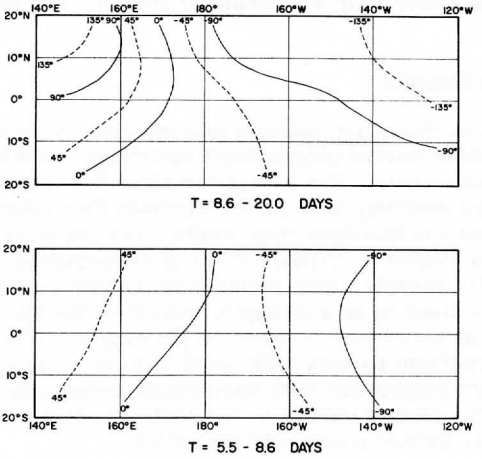

Figure 9. Spatial distribution of cloud-cover coherency phase for separate frequency bands. Phase is taken from cloud-cover coherency at each point relative to zone S4.

except at high frequencies, the magnitudes are relatively large, allowing some confidence in the significance of the phases. The middle frequency band exhibits the most clear-cut westward propagation, with no substantial meridianal component evident. The spacing of the phase lines indicates a planetary wavelength of approximately 160° longitude, corresponding to a propagation speed of 23° longitude per day for a seven-day period.

A similarly large wavelength is apparent in the Southern Hemisphere for the lowest frequencies, where the apparent westward phase propagation is 15° longitude per day. However, the wavelength in the northwest portion of the area decreases to about 50°, indicating a westward phase speed of 4° longitude per day.

Since coherency magnitudes are smaller at the high frequencies, the phase estimates are less reliable. In addition, the large (20°) longitudinal distance between sectors precludes easy analysis of the small-scale traveling cloud clusters. Nevertheless, a tally of narrow-band coherencies for periods in the vicinity of four days showed that the phases for the most significant estimates were mainly in the range 300° – 420°. Assuming that a single wave mode is involved, a mean wavelength of about 2,000 km. is indicated for these four-day periods. However, a note of

caution is needed, since a phase of 420° may be interpreted as only 60°, corresponding to a very long wavelength of about 12,000 km.

4. Concluding Remarks

The results of this study indicate that the cloud activity over the Central Pacific exhibits marked geographical variations, both in its persistent and transient components. The associated statistical patterns suggest that the belts of major activity, such as the Northern Hemisphere ITCZ, consist of both persistent and transient components, with the transient fluctuations apparently being related to different kinds of disturbances, depending upon the location. For example, long-period activity with a period of about eleven days was found to be a maximum away from the equator, in contrast to the four-day periods found centered on the equator. The systems with longer and intermediate periods were found to behave more coherently, exhibiting westward propagation with wavelengths ranging up to 160° longitude. The shorter periods were less coherent, and only a tentative estimate of a considerably shorter wavelength was given.

The difficulty with this latter estimate helps to bring out an important limitation of this spectral approach, namely that the entire temporal behavior is characterized by only a single statistical quantity. It is clear that this is incapable of characterizing systematic slow changes (for example, seasonal) or intermittency in the disturbances in a given frequency band. In addition, the usefulness of the technique in estimating wavelengths and phase speeds is naturally limited to systems whose given frequency band is associated with a single longitudinal wavelength alone. Thus the method lacks precision when applied to a study of the ITCZ, at least to the extent that the ITCZ fluctuations reflect both easterly-wave and planetary-wave scales. An alternative approach using band-filtered time series is currently being tested by the authors.

The present work could also be improved by more refined data types and networks. For example, increased spatial resolution would allow more precise study of the ITCZ and cloud-cluster systems. The use of cloud brightness enhancement techniques and wind data would help focus upon the more active cloud groupings. Finally, seasonal and inter-annual variations could be studied using extended time series. Some studies along these lines are currently underway.

Acknowledgments

The authors wish to thank Mr. Peter Guetter, who provided valuable assistance with computer programming problems arising in this study. This research was sponsored by NASA under Contract No. 11542 and by ESSA grant E-230-68-(9).

References

1. Blackman, R. B. and J. W. Tukey, 1958: The measurement of power spectra from the point of view of communications engineering, Dover Publication (New York), 190.

2. Chang, C. P., 1970: Westward Propagating Cloud Patterns in the Tropical Pacific as seen from Time-Composite Satellite Photographs. J. Atmos. Sci. 27, 133-138.

3. Hubert, L. F., A. F. Krueger, and J. S. Winston, 1969: The Double Intertropical Convergence Zone—Fact or Fiction? J. Atmos. Sci. 26, 771-773.

4. Kornfield, J., A. F. Hasler, K. J. Hanson and V. E. Suomi, 1967: Photographic Cloud Climatology from ESSA III and V computer produced mosaics. Bull. Amer. Meteor. Soc., 48, 878-883.

5. Maruyama, T., 1968: Time series of power spectra of disturbances in the equatorial lower stratosphere in relation to quasi-biennial oscillation. J. Meteor. Soc. Japan, 45, 404-417.

6. Nitta, T., 1970(a): Statistical Study of Tropospheric Wave Disturbances in the Tropical Pacific Region. J. Meteor. Soc. Japan, 48, 47-59.

7. Nitta, T., 1970(b): On the role of transient eddies in the tropical troposphere. J. Meteor. Soc. Japan, 48, 348-359.

8. Palmer, C. E., 1951: Tropical Meteorology. Compendium of Meteorology, Boston Amer. Meteor. Soc., 859-880.

9. Panofsky, H. A. and G. W. Brier, 1965: Some applications of statistics in Meteorology, Penn. State University.

10. Riehl, H., 1945: Waves in the easterlies and the polar front in the tropics. Dept. of Meteorology, University of Chicago, Misc. Rept. 17.

11. Riehl, H., 1954: Tropical Meteorology. New York, McGraw-Hill.

12. Rosenthal, S. L., 1960: Some estimates of the power spectral of large-scale disturbances in low latitudes. J. Meteor. 17, 259-263.

13. Sikdar, D. N. and V. E. Suomi, 1970: Time variation of tropical energetics as estimated from geostationary satellite altitude. Accepted for publication in the J. Atmos. Sci.

14. Wallace, J. M. and C. P. Chang, 1969: Spectrum analysis of large-scale wave disturbances in the tropical lower troposphere. J. Atmos. Sci., 26, 1010-1025.

15. Yanai, M. and T. Maruyama, 1966: Stratospheric wave disturbances propagating over the equatorial Pacific. J. Meteor. Soc. Japan, 44, 291-294.

16. Yanai, M., T. Maruyama, T. Nitta, and Y. Hayashi, 1968: Power spectra of large-scale disturbances over the tropical Pacific. J. Meteor. Soc. Japan, 46, 308-323.

17. Yanai, M., and M. Murakami, 1970: A further study of tropical wave disturbances by the use of spectrum analysis. J. Meteor. Soc. Japan, 48, 185-197.

The Effects of Shear and Temperature Distribution on Low-level Convection

by David Suchman and John A. Young

Abstract:

Investigations are made of some features of perturbations superimposed on a plane parallel flow with unstable thermal stratification and variable vertical wind shear. A set of linearized Boussinesq equations governing the flow are solved numerically by finite difference methods. The aspects of the perturbations studied are growth rates and phase speeds (obtained from the eigenvalues), and structural characteristics of the vertical velocity and temperature perturbation fields (obtained from the eigenvectors); the heat flux associated with the temperature-velocity correlation is also studied.

It is found that a constant wind shear exerts a stabilizing effect on the thermal instabilities, as does a variable wind shear. The effects of the latter are less pronounced, however.

The dependence on mean thermal stratification appears to be much stronger than the wind shear dependence. The existence of temperature inversions obscures the damping caused by a constant wind shear. It also strongly concentrates the temperature perturbation field in a smaller region below the stable layer. The base height of the stable region, and not the strength of the inversion, proves to be the crucial parameter.

The latter sections are devoted to a discussion of the effects of relating the base-state temperature and wind fields in a qualitatively realistic manner. The strength and distribution of the wind shear does not prove to be important in the thermally stable regions, but its magnitude is very significant for damping in the thermally unstable region. No set of environmental conditions was found to be more ideal for the production of convective instabilities than the case with zero mean wind shear and static thermal instability.

1. Introduction

The study of instabilities produced by unstable thermal stratification and by vertical wind shear has been pursued by meteorologists and fluid dynamicists for over half a century. More recently, meteorologists have become very interested in studies of the boundary layer, the lowest atmospheric region which directly affects man. Among the phenomena characteristic of this layer are vertical wind shear, unstable thermal stratification and temperature inversions. All of the above three have an important relationship to the form and strength of thermal or convective instabilities near the surface.

The first convection problem studied was that of simple Benard convection (Jeffreys, 1928) which is characterized by an unstable temperature stratification in the vertical, leading to cellular motions. Lord Rayleigh (1916) set forth the idea that the Benard problem was really a stability problem, and established the criterion for the onset of simple convection. Pellew and Southwell (1940) generalized the convection theory to include different upper and lower boundary conditions, and clarified the nature of the various cellular formations observed. It was later observed (Stommel, 1948) that the Rayleigh number (Ra) played an important role in determining the form of the instability produced. As Ra increases, the state of thermal conduction proceeds to one of steady cellular motions, then on to aperiodic, irregular and finally turbulent motion. In all of the above studies, no mean wind shear was present.

Ingersoll (1966, 1966a) performed mathematical studies where both temperature and velocity gradients existed in the fluid, the latter of which were produced by moving the bounding surfaces relative to each other. When shear was present, the longitudinal rolls which formed were found to be unstable above a critical Rayleigh number larger than 1708, which is that found for the case of zero wind shear. Hence, the basic conductive state was disturbed in these cases. As the Reynolds number (Re) was increased, the wavelength of the most unstable disturbance also increased, while its growth rate decreased.

Schlichting (1968) describes two types of atmospheric instabilities which are caused by the action of wind shear. One is produced by an inflection point in the velocity profile. Asai (1969) studied this type of "shear" instability in a thermally unstable environment. A second, similar type of instability is the viscous or Tollmein-Schlichting instability; in its simplest form it occurs for flow along a flat plate with zero pressure gradient in the horizontal.

Lilly (1966) studied two kinds of instabilities in a neutrally stratified Ekman boundary layer. One type was associated with an inflection point

in the velocity profile and occurred at high Re; another ("parallel instability") was caused by a mechanism involving an interaction between Coriolis and viscous effects at low Re.

Faller (1965) and Faller and Kaylor (1966) made studies of the interrelationship between convective and shear instabilities in the "real" atmosphere. In agreement with Lilly (1966) they found that shear in the atmospheric boundary layer could produce unstable motions which were not associated with thermal processes. (Even with a stable stratification, a large enough mean wind in the real atmosphere through the action of the small-scale turbulence might destroy the stratification, thus producing larger-scale unstable perturbations.)

Asai (1969a) showed that a constant vertical wind shear stabilized convective instabilities, and that either of two different modes of instabilities (a stationary wave, and "twin" transitive waves) were established, depending upon the wavelength. He later (1969) examined the role of variable vertical shear, and showed its effects to be somewhat weaker than that found for a constant wind shear when the same Richardson number is taken for both cases.

All of the above studies examined the influence of shear in the presence of constant temperature lapse rates. The present study is an attempt to extend their work by examining the role of variable basic temperature (including those with inversions) and wind structures in the basic linear theory. The basic method of analysis is based upon that used by Asai (1969a) in which the eigenvalue equations are transformed into finite difference form and solved numerically. A special effort is made to specify basic wind and temperature distributions which resemble those of the real atmosphere. It is found that variation of those parameters causes marked changes in the growth rates, phase speeds and vertical structure of temperature and vertical motion profiles in the instabilities produced.

The case without wind shear is presented as a reference point in Chapter 3. In Chapter 4, with a constant shear and constant temperature lapse rate present, the long and short wavelength regimes, and the transition zone between them, are examined in detail. Chapter 5 deals with rhe results of varying the magnitude of a constant lapse rate. The effects of temperature inversions on both the zero-shear and constant-shear cases are examined in Chapter 6. Next, the consequences of a two-dimensional vector wind shear, where the wind turns with height, on both the constant lapse rate and the inversion temperature distributions is discussed. In Chapters 8 and 9, the wind and temperature fields are coupled in a realistic manner such that greater thermal stability accompanies stronger vertical wind shear.

2. Formulation and Solution of the Problem

Basic Equations

Let us consider a viscous fluid layer which is bounded by two horizontal planes at $z = 0$, $z = h$ in a nonrotating coordinate system. We take z to be the vertical axis. We assume a base-state velocity distribution of:

$$\bar{U} = \bar{U}_0 + \Lambda z \tag{2.1}$$

where U_0 is velocity at $z = 0$, and Λ is a function of z. Thus, the vertical wind shear in the x-direction is

$$\frac{\partial \bar{U}}{\partial z} = \Lambda + z \frac{\partial \Lambda}{\partial z} \tag{2.2}$$

We make an analogous assumption for the mean velocity in the y-direction:

$$\bar{V} = V_0 + \pi z \tag{2.3}$$

The basic temperature distribution is assumed to be

$$\bar{T} = T_0 - \Gamma z \tag{2.4}$$

where T_0 is the temperature at $z = 0$, and Γ is a function of z also. Hence, the lapse rate is

$$\frac{\partial \bar{T}}{\partial z} = -(\Gamma + z \frac{\partial \Gamma}{\partial z}) \tag{2.5}$$

The density is assumed to be

$$\bar{\rho} = \rho_0 \{1 - \alpha(\bar{T} - T_0)\} \tag{2.6}$$

where ρ_0 is the density at the lower boundary.

The pressure field $\bar{p}$ can be derived from the hydrostatic equation

$$\frac{\partial \bar{p}}{\partial z} = -g\bar{\rho} \tag{2.6a}$$

where g is the gravitational acceleration, and α is the coefficient of thermal expansion.

A Boussinesq approximation which is accurate for shallow convection will be used, i.e., ρ_0 = constant except in Eq. (2.9).

The linearized perturbation equations are then:

$$\frac{\partial u'}{\partial t} + \bar{U}\frac{\partial u'}{\partial x} + \bar{V}\frac{\partial u'}{\partial y} + w'\frac{\partial \bar{U}}{\partial z} = -\frac{1}{\rho_0}\frac{\partial p'}{\partial x} + \nu\nabla^2 u' \tag{2.7}$$

$$\frac{\partial v'}{\partial t} + \bar{U}\frac{\partial v'}{\partial x} + \bar{V}\frac{\partial v'}{\partial y} + w'\frac{\partial \bar{V}}{\partial z} = -\frac{1}{\rho_0}\frac{\partial p'}{\partial y} + \nu\nabla^2 v' \tag{2.8}$$

$$\frac{\partial w'}{\partial t} + \bar{U}\frac{\partial w'}{\partial x} + \bar{V}\frac{\partial w'}{\partial y} = -\frac{1}{\rho_0}\frac{\partial p'}{\partial z} + g\alpha T' + \nu\nabla^2 w' \tag{2.9}$$

$$\frac{\partial u'}{\partial x} + \frac{\partial v'}{\partial y} + \frac{\partial w'}{\partial z} = 0 \tag{2.10}$$

$$\frac{\partial T'}{\partial t} + \bar{U}\frac{\partial T'}{\partial x} + \bar{V}\frac{\partial T'}{\partial y} + w'\frac{\partial \bar{T}}{\partial z} = \kappa\nabla^2 T' \tag{2.11}$$

where u', v' and w' are the velocity components in the x, y and z directions, T' and p' are the temperature and pressure of the perturbation respectively, ν is the coefficient of kinematic viscosity, κ is the coefficient of the thermometric conductivity, and ∇^2 denotes the three-dimensional Laplacian operator.

By combining equations (2.7) - (2.10) and eliminating u', v' and p', we obtain the following equations for w' and T' (from Eq. (2.11)).

$$\left\{\frac{\partial}{\partial t} + \bar{U}\frac{\partial}{\partial x} + \bar{V}\frac{\partial}{\partial y} - \nu\nabla^2\right\}\nabla^2 w' - g\alpha\nabla_H^2 T' - \frac{\partial^2 \bar{U}}{\partial z^2}\frac{\partial w'}{\partial z} - \frac{\partial^2 \bar{V}}{\partial z^2}\frac{\partial w'}{\partial y} = 0 \tag{2.12}$$

$$\left\{\frac{\partial}{\partial t} + \bar{U}\frac{\partial}{\partial x} + \bar{V}\frac{\partial}{\partial y} - \kappa\nabla^2\right\}T' + w'\frac{\partial \bar{T}}{\partial z} = 0 \tag{2.13}$$

where $\nabla_H^2 = \frac{\partial^2}{\partial x^2} + \frac{\partial^2}{\partial y^2}$.

Boundary Conditions

It is assumed that the upper and lower boundary surfaces are fixed and smooth. Thus, the normal components of the velocity w' as well as the tangential stresses must vanish at the boundaries. Using (2.10) and the definition of the stress tensor, we obtain:

$$w' = \frac{\partial^2 w'}{\partial z^2} = 0 \qquad \text{at } z = 0 \text{ and } z = h \tag{2.14}$$

In addition, we will assume that constant temperatures are maintained at both the upper and lower boundaries:

$$T' = 0 \qquad \text{at } z = 0 \text{ and } z = h \tag{2.15}$$

Formulation of the Problem

Since the coefficients in the linear equations (2.12) and (2.13) vary only in z, we may assume sinusoidal solutions of the form

$$w' = W(z) \exp\{i(kx + \ell y) + \sigma t\} \tag{2.16a}$$

$$T' = \theta(z) \exp\{i(kx + \ell y) + \sigma t\} \tag{2.16b}$$

where k and ℓ are the wavenumbers in the x and y directions, respectively. W(z) and $\theta(z)$ are complex functions, reflecting variable amplitudes and phases. The real part of σ denotes the amplification rate, while the imaginary part reflects horizontal phase propagations.

Next, we define the following dimensionless quantities, denoted by the superscript * .

$$\begin{aligned}
&\sigma = \sigma^* \nu h^{-2} \\
&k = k^* h^{-1}, \quad \ell = \ell^* h^{-1}, \quad z = z^* h \\
&W = W^* \nu / h \\
&\bar{U} = \bar{U}^* \Lambda_0 h, \quad \bar{V} = \bar{V}^* \Lambda_0 h \\
&\theta = \theta^* \Gamma_0 h \\
&\bar{U}_z = \Lambda_0 U^*_{z^*}, \quad \bar{V}_z = \Lambda_0 V^*_{z^*}, \quad \bar{T}_z = \bar{T}^*_{z^*} \Gamma_0
\end{aligned} \tag{2.17}$$

Γ_0 and Λ_0 are taken as positive constants.

We will also define

$$K^{*2} = k^{*2} + \ell^{*2}$$

Substituting (2.16a) and (2.16b) into (2.12) and (2.13), and using (2.17) we obtain

$$\{\sigma^* + iRe\,k^*\bar{U}^* + iRe\,\ell^*\bar{V}^* - (\frac{d^2}{dz^{*2}} - K^{*2})(\frac{d^2}{dz^{*2}} - K^{*2})\}W^*$$

$$+ Pr^{-1}RaK^{*2}\theta^* - (iRe\,k^*\frac{\partial^2\bar{U}^*}{\partial z^{*2}} + iRe\,\ell^*\frac{\partial^2\bar{V}^*}{\partial z^{*2}})W^* = 0 \qquad (2.18)$$

$$\{\sigma^* + iRe\,k^*\bar{U}^* + iRe\,\ell^*\bar{V}^* - (\frac{d^2}{dz^{*2}} - K^{*2})\,Pr^{-1}\}\theta^* + W^*\frac{\partial\bar{T}^*}{\partial z^*} = 0 \qquad (2.19)$$

where:

Prandtl number: $Pr = \nu/\kappa$

Rayleigh number: $Ra = g\alpha\Gamma h^4/\kappa\nu$

Reynolds number: $Re = \Lambda h^2/\nu$

For our purposes we will use the Richardson number, Ri, instead of Re, and it will be defined by the equation

$$Ri = (Ra/Pr \cdot (Re)^2)$$

As defined above, the sign of the Richardson number is opposite that which is commonly used; i.e., $Ri = g\alpha\Gamma_0/\Lambda_0$.

Unless otherwise noted, Pr = 7 (which is approximately equal to that for water at s.t.p.), $Ra = 10^5$ which is far above the critical value needed for convection to take place (Ingersoll, 1966), Ri = 1.0, and hence Re = 120 (sufficient for the shear flow to have an effect on the convection) (Faller and Kaylor, 1966).

Nondimensionalization of the boundary conditions yields,

$$W^* = \frac{d^2W^*}{dz^{*2}} = 0 \quad \text{at } z^* = 0 \text{ and } z^* = 1 \qquad (2.20)$$

$$\theta^* = 0 \quad \text{at } z^* = 0 \text{ and } z^* = 1 \qquad (2.21)$$

Numerical Procedure

The set of ordinary differential Eqs. (2.18) and (2.19) is transformed to a set of algebraic equations by use of a finite difference scheme to approximate the vertical derivatives of W^* and θ^*. The fluid, which has

a nondimensionalized depth of unity, is divided into n sublayers with equal nondimensional thickness 1/n. For our purposes, we chose n = 16, as Asai (1969a) showed that this value of n yielded accurate results for the primary unstable modes.

The perturbation derivatives with respect to z^* are approximated by a centered difference quotient as follows:

$$\left(\frac{dW^*}{dz^*}\right)_j \simeq n/2(W^*_{j+1} - W^*_{j-1}) \tag{2.22}$$

$$\left(\frac{d^2W^*}{dz^{*2}}\right)_j \simeq n^2(W^*_{j+1*} - 2W^*_{j*} + W^*_{j-1*}) \tag{2.23}$$

The subscript j denotes the interior level at which the derivatives are taken: $j = 1, \ldots, (n-1)$. $j = 8$ is the mid-level.

At the j^{th} level, Eq. (2.18) reduces to

$$-n^4W^*_{j-2} + C_jW^*_{j-1} - D_jW^*_j + C_jW^*_{j+1} - n^4W^*_{j+2} + Pr^{-1}RaK^{*2}\theta_j^* = 0 \tag{2.24}$$

while Eq. (2.19) becomes

$$n^2Pr^{-1}\theta^*_{j-1} - E_j\theta^*_j + n^2Pr^{-1}\theta^*_{j+1} - W^*_j\left(\frac{d\bar{T}^*}{dz^*}\right)_j \tag{2.25}$$

where:

$$C_j = in^2Re\,k^*\bar{U}^*_j + in^2Re\,\ell^*\bar{V}^*_j + 4n^4 + 2n^2K^{*2} + n^2\sigma^*$$

$$D_j = iRe(2n^2 + K^{*2})k^*\bar{U}^*_j + iRe(2n^2 + K^{*2})\ell^*\bar{V}^*_j + 6n^4 + 4n^2K^{*2}$$
$$+ (2n^2 + K^{*2})\sigma^* + K^{*4} - (2n^2 + K^{*2})\left\{iRe\,k^*\frac{\partial^2\bar{U}^*}{\partial z^{*2}} + iRe\,\ell^*\frac{\partial^2\bar{V}^*}{\partial z^{*2}}\right\}$$

$$E_j = iRe\,k^*\bar{U}^*_j + iRe\,\ell^*\bar{V}^*_j + Pr^{-1}(2n^2 + K^{*2}) + \sigma^*.$$

The temperature and velocity distributions of the environment $\bar{U}^*$, $\bar{V}^*$,

and $\partial\bar{T}^*/\partial z^*$ are specified beforehand.

The conditions at the upper and lower boundary, Eqs. (2.20) and (2.21) now become:

$$\begin{aligned} W_0^* &= W_n^* = 0 \\ W_{-1}^* + W_1^* &= 0 \\ W_{n-1}^* + W_{n+1}^* &= 0 \\ \theta_0^* &= \theta_n^* = 0. \end{aligned} \tag{2.26}$$

W_{-1} and W_{n+1} are used only to simplify (2.24) using the relations (2.26). The set of finite difference equations, (2.24) and (2.25), constitute $2(n-1)$ linear equations in the same number of unknown complex variables W_ℓ^* and θ_ℓ^* $(\ell = 1, 2, \ldots, n-1)$.

We can write them in matrix form,

$$(A - \sigma^* B)X = 0 \tag{2.27}$$

where A and B are matrices with complex elements, and X is the corresponding eigenvector solution for W^* and θ^* for each eigenvalue σ^*.

Multiplying (2.27) by the inverse of B, we obtain

$$(B^{-1}A - \sigma^* I)X = 0 \tag{2.28}$$

where I is the unit matrix and B^{-1} is the inverse of B.

Under the restriction that X is a nonzero solution, the determinant of the matrix $(B^{-1}A - \sigma^* I)$ must vanish, i.e.,

$$|B^{-1}A - \sigma^* I| = 0. \tag{2.29}$$

This eigenvalue problem yields a frequency equation for σ^*, which may be complex. A real part of σ^* represents an amplification rate of the perturbation amplitude, and the imaginary part of σ^* (σ_i^*) gives the horizontal phase speed. In this study we consider the trace speed of the instability in the x-direction related to σ by $C_x^* = -\sigma_i^*/k^*$, etc.

After obtaining σ^*, the eigenvectors for W^* and θ^* are obtained, and are unique except for an arbitrary constant of multiplication.

Using the solution obtained above, we will investigate the structure, stability characteristics and vertical heat flux of the perturbations. The main structural characteristics examined will be the maximum value of θ^*, the shape in the vertical of the $|W^*|$ and $|\theta^*|$ fields and their tilts. The tilt of the W^* perturbation field at a point is related to vertical variations in the phase $\epsilon_W = \tan^{-1}(W_i^*/W_r^*)$. A forward tilt will have $W_i^* > 0$ in the lower layers in the cases studied here. The eigenvectors are normalized such that $|W|$ max = 1.0. From (2.16a)

$$w' = \mathrm{Re}[W^* e^{\{i(kx+\ell y) + \sigma t\}}] = |W^*| \cos\{(kx+\ell y) + \sigma t + \epsilon_w\}$$

From (2.16b),

$$T' = \mathrm{Re}[\theta^* e^{\{i(kx+\ell y) + \sigma t\}}] = |\theta^*| \cos\{(kx+\ell y) + \sigma t + \epsilon_\theta\}$$

The heat flux will be defined as

$$\overline{w'T'}^{x,y} = |\theta^*||W^*| \{\cos\{(kx+\ell y)+\sigma t\} + \epsilon_\theta(z)\}\{\cos\{(kx+\ell y)+\sigma t\}+\epsilon_w(z)\}$$

where the overbar denotes a horizontal average. The product of the cosine terms represents the correlation of w' and T'. When ϵ_θ and ϵ_w vary in the same way (the tilts are the same), the correlation is a constant.

3. Constant Wind Case

The initial study made was of cases with no vertical wind shear, where a constant mean wind was present in the x-direction, and the environmental wind was zero in the y-direction. The two cases studied were $k^* = \ell^* = 1.0$, and $k^* = \ell^* = 3.0$.

At least two growing modes were observed, the number depending upon the wavelength. For $\partial\bar{T}^*/\partial z^* = -1.0$, two unstable modes were observed for the long wavelength case, though both had the same magnitude of phase speed. The faster-growing instability was symmetric about the mid-level, where maxima in the amplitudes $|W^*|$ and $|\theta^*|$ occurred. As with all cases studied, the warm cores coincided with the axis of upward motion for the unstable modes. Thus, the vertical heat flux was large. The less unstable mode possessed double $|W^*|$ and $|\theta^*|$ maxima located at $z^* = 1/4$ and $z^* = 3/4$ and each had continuous forward tilts with a net phase difference of 180°. The θ^* field was stronger than that of the other mode, and the w' - T' correlation was large.

When $k^* = \ell^* = 3.0$, three unstable perturbations were found. The two most unstable ones were related to the two modes discussed above, and the structure of the least unstable one resembled that of the fastest growing mode. The maximum value of the θ^* field was inversely related to the growth rate of the three modes. The growth rates were larger for the shorter wavelengths, all other conditions being equal.

As the magnitude of the constant lapse rate increased, the growth rate of the unstable modes also increased, as did the relative value of the θ^* maximum. Doubling the lapse rate caused less than a doubling of the growth rates, however.

All further studies will be built upon this one, and the simple cellular patterns will become much more complex, as the temperature and mean wind fields are varied.

4. Wavelength Regimes for the Constant Shear Case

When a constant-shear profile is introduced, two main changes from the previous case are readily observed. First, shear exerts a suppressing influence on the growth of the unstable perturbations as well as reducing the number of unstable modes (Asai, 1969a), and second, there are two distinct wavelength regimes. In the following,

$$k^* = \ell^*, \quad \frac{\partial \bar{T}^*}{\partial z^*} = -1.0, \quad \frac{\partial \bar{U}^*}{\partial z^*} = +1.0, \text{ and } \bar{U}_0 = 0.$$

In the region where $K^* \leq 1.8$, the long wavelength regime was found, in which only one unstable mode was present for each wavelength, and the growth rates gradually increased with the wavenumber. The phase speeds remained relatively constant in the entire region studied. As shown in Figure 1a, the W field was perfectly symmetric, with a maximum value occurring at mid-level. The vertical tilt was moderate, and with the same direction was the prevailing wind shear. The θ^* field (see Figure 5) is also symmetric, with a maximum value at mid-level also. Its tilt was in the same direction, but twice as large as W^*. W^* and θ^* were strongly correlated, indicating a large net heat flux upward.

The region of transition was for $1.8 \leq K^* \leq 2.05$, as may be noticed in Figure 2. Two instabilities now appear with the larger growth rate decreasing and the smaller one increasing as K^* increases. The phase speeds are initially the same, but gradually they begin to diverge. The W^* field, from Figure 1b, continues to be symmetric with a $|W^*|$ maximum still at mid-level. The instability with the slower growth rate has a larger tilt, but the difference decreases, as we continue to increase the wave number. The same is true about the tilt of the θ^* field, and, as

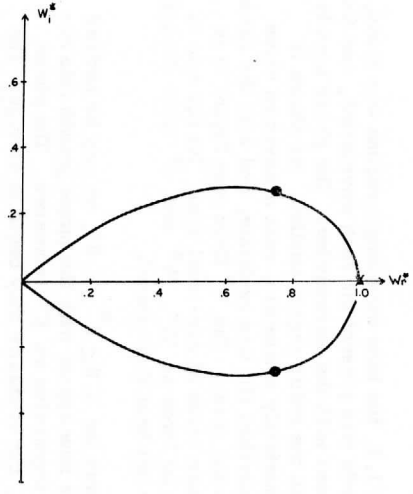

Figure 1a. Hodograph of W^* for the case where the vertical wind shear is constant, $-\partial\bar{T}^*/\partial z^* = 1.0$, and $k^* = \ell^* = 1.2$. The levels $z^* = .313$, and $z^* = .688$ are indicated by dots, $z^* = .500$ is shown by a cross. Height increases clockwise.

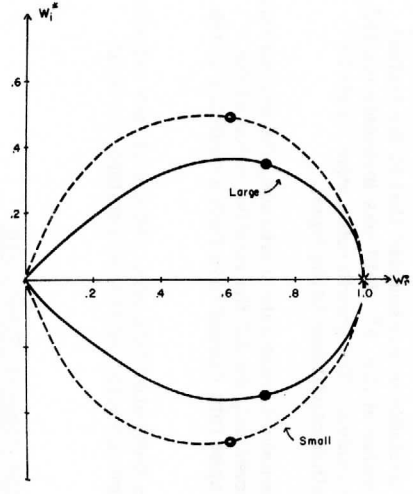

Figure 1b. Same as Figure 1a, except $k^* = \ell^* = 1.4$. Both growth modes are indicated.

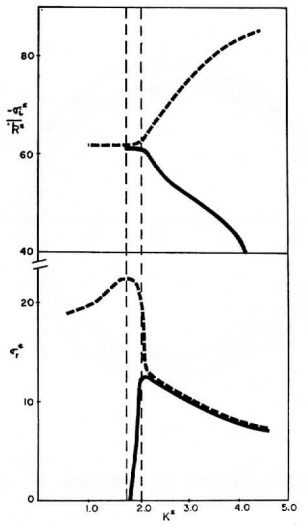

Figure 2. Growth rates and trace speeds in the x-direction as a function of K^* for the constant wind shear case and $-\partial\bar{T}^*/\partial z^* = 1.0$.

with the case before, the values to which the tilts converge increase with K^*. As with the long waves, the $W^* - \theta^*$ correlation is high.

As we continue to increase the value of K^*, we enter the short wavelength regime. The growth rates of the two instabilities become the same (see Figure 2) and we continue to have these dual unstable modes as K^* increases, but their growth rates become smaller. The phase speeds continue to diverge from one another, each reflecting the strength of the mean wind field at the level of its maximum $|W^*|$. From Figures 3 and 4, we notice that the W^* fields are no longer symmetric about the mid-level, and the former shows that the two unstable modes are mirror images of each other (only one mode for each wavelength is shown in Figure 4 for $K^* = 4.24$). The tilt becomes more concentrated in one vertical layer, and as K^* increases the level of maximum W^* departs further from mid-level. They appear at $z^* = 1/3$ and $z^* = 2/3$ for the twin instabilities when $K^* = 4.24$. The total tilt of the W^* field is greater for short wavelengths than for long wavelengths.

Figure 6 shows the structure of the θ^* field for the short wavelength mode. As with W^*, the symmetry of the field is lost, two mirror image instabilities are found, and the maxima are found above and below the mid-

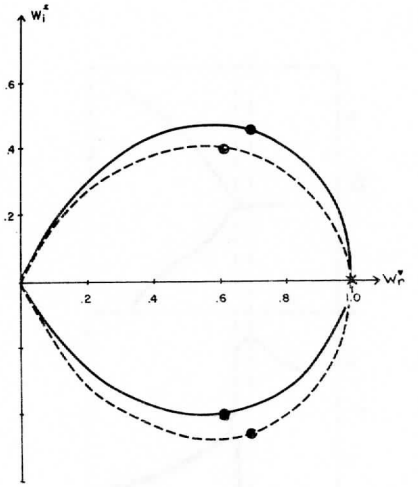

Figure 3. Same as Figure 1a, except $k^* = \ell^* = 1.5$.

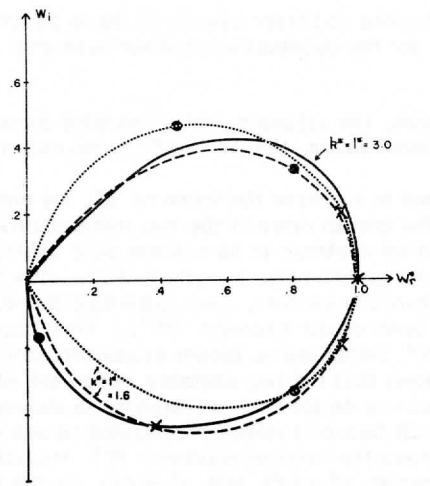

Figure 4. Same as Figure 1a, except for $k^* = \ell^* = 1.6$, and $k^* = \ell^* = 3.0$.

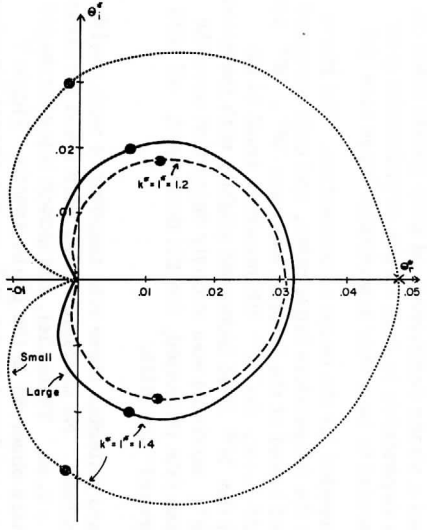

Figure 5. Hodograph of θ^* for the case where the vertical wind shear is constant, $-\partial\bar{T}^*/\partial z^* = 1.0$, and $k^* = \ell^* = 1.2, 1.4$. Other features are the same as Figure 1a.

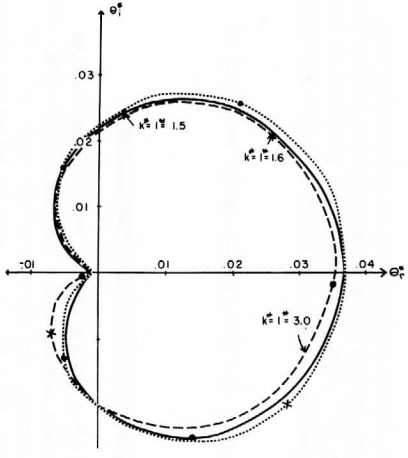

Figure 6. Same as Figure 5, except $k^* = \ell^* = 1.6, 3.0$.

level, respectively. The relative strength of the θ^* field is greater for K^* large than when it is small. The $W^* - \theta^*$ correlation continues to remain high, but now we have the maximum heat flux occurring in the lower layers for one unstable mode, and in the upper layers for the other unstable mode. The instability whose maxima appear in the lower layers is the one that moves at the slower speed.

The inclusion of shear in the model produces many differences from the no-shear case: the number and growth rates of the unstable modes are reduced, tilts are created in the W^* and θ^* fields, the structure of the instability becomes dependent upon wavelength, and the relative strength of the θ^* field is enhanced.

For the short wavelength cases, the distribution of the heat flux is also altered.

5. Lapse Rate Magnitude Variations for Constant Shear Case

Having examined the effect of constant shear, we next look at the dependence of the instability on the strength of a constant lapse rate. The same shear profile will be used again, and all cases will have $k^* = \ell^*$. Unless otherwise stated, the case $k^* = \ell^* = 1.0$ will be taken as representative of the long wavelength instability, and $k^* = \ell^* = 3.0$ as representative of the short wavelength modes. The lapse rates studied ranged from $-\partial\bar{T}^*/\partial z^* = +0.33$ to $-\partial\bar{T}^*/\partial z^* = +1.5$. When $-\partial\bar{T}^*/\partial z^* = 0.0$ through the entire layer, no unstable modes appear.

The long waves showed a strong dependence of their growth rates on the lapse rate, though the dependence is less as the stratification grew more unstable. There appeared to be a very low critical lapse rate (of $0.0 < -\partial\bar{T}^*/\partial z^* < 0.33$) needed for the onset of convection. The phase speed was independent of the temperature lapse rates, and only appeared to depend on the mean wind speed at the level of maximum W^*. W^* and θ^* maxima remained at mid-level, the W^* tilt remained small in all cases, but the strength of the W^* field increased slightly with the growth rate. The value of the $|\theta^*|$ maximum was strongly dependent upon the lapse rate, and as the lapse rate increased, the tilt decreased; all tilts continued to be in the "forward" direction.

The short-wave regimes reflected lapse rate magnitudes more readily than did the long-wave regimes. No unstable modes were found for lapse rates less than $-\partial\bar{T}^*/\partial z^* = 0.66$. Thereafter, the growth rates increased rapidly. Little variation was observed in the phase speeds. Figure 7 shows that little change was produced in the W^* profile except for minor

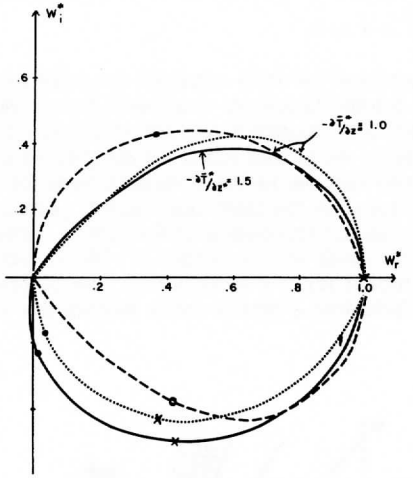

Figure 7. Same as Figure 1a, except $k^* = \ell^* = 3.0$, and $-\partial\bar{T}^*/\partial z^* = 1.0$, 1.5.

alterations in the distribution of the tilt. The θ^* field behaved in a similar manner as was observed for the long wavelength cases. Since the $|\theta^*|$ maximum was increasing, and the $\theta^* W^*$ correlation was fairly constant, the heat flux increased with the lapse rate.

The existence of a constant wind shear lessened the influence of thermal stratification on convection, but the lapse rate still appeared to be a controlling factor in determining whether instabilities would be found. Even under very unstable conditions, growth rates were drastically reduced by the shear, especially in the short wavelength cases, and small instabilities entirely eliminated.

6. Temperature Inversions with Constant Shear

Figure 8 shows the various temperature profiles which were used for the studies of this chapter, and compares them with the "basic cases" discussed earlier. A lapse rate of $-\partial\bar{T}^*/\partial z^* = +1.5$ was specified in the lower, unstable regions to insure the creation of unstable modes with an inversion present; in this way the effects of the height and strength of the inversion could be isolated and studied easier. Once again, all cases

were for constant vertical wind shear, $k^* = \ell^*$ (unless otherwise indicated), and $\partial \bar{U}^*/\partial z^* = +1.0$.

As a control experiment we first consider the case where no shear was present. All studies for the longwave case were for strong inversions. The growth rates appeared to be in direct relation to the height of the inversion base. Only one unstable mode was found for inversions below $z^* = .625$. $|W^*|$ maxima appeared just below the inversion base for low inversions and rose at a lesser rate than the inversion height. Little tilt was observed, although there was an abrupt truncation of the $|W^*|$ field. The point of $|\theta^*|$ maximum behaved analogously to that of $|W^*|$, but the maximum amplitude was much higher for low inversions. The inversion appears to concentrate the θ^* field into a smaller area (within the unstable region),

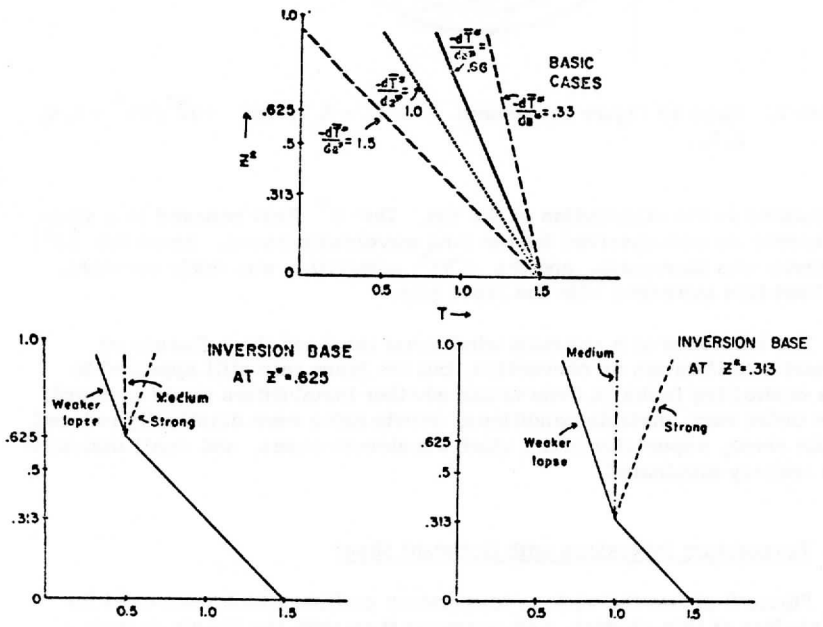

Figure 8. The base-state temperature distributions examined in this study.

and abruptly truncates it when a stable thermal stratification is encountered. The heat flux is thus more intense in low layers when an inversion is present, but it decreases rapidly with height in the inversion layers.

For the shortwave case without shear, the height, rather than the strength, of the inversion was the most important parameter. With the exception of the weak inversion case, the low inversion only permitted one unstable mode, while the high inversion allowed two. For only in the case where the inversion was weak did we find modes whose maxima appear in the stable layer; these were not the fastest growing modes, however. No obvious explanation seems apparent for this phenomenon. The general structures of the short wavelength instabilities were analogous to the other case (just discussed), as tilt in the vertical still did not appear; the growth rates were much larger here than for the long wavelength perturbations under similar conditions. The only other obvious differences were: a) the existence of double $|\theta^*|$ maxima (one within the stable layer) for the slower growing unstable modes, and b) the changes produced by altering the inversion strength were more pronounced than before.

Next, a constant vertical shear of the $\bar{U}$ wind was allowed. For the long wavelength case, the inversions had no truncating effect on the W^* field (see Figure 9). The tilt varied inversely with the shear strength. The high inversion did not greatly alter the point of $|W^*|$ maximum, while the vertical motion was greatest in the lower part of the stable layer for the low inversion. Growth rates were only altered by changes in the height of the base of the stable layer.

In the case of the long waves, the inversion produced a marked truncation in the θ^* field and altered its general structure. The low inversion concentrated the field strength into the lowest layers and the $|\theta^*|$ maximum was greatly increased. The high inversion produced the same changes, but they were much less marked. Figure 10 shows a comparison between the constant-lapse-rate case and the inversion case; the truncation at the inversion point is very evident. For the long wavelength case, the temperature inversions alter the structure of the θ^* field thus lowering the $W^* - \theta^*$ correlation, and hence the heat flux is greatly reduced.

For the short waves, the low inversion only permits one unstable mode, while two instabilities are found when the base of the stable layer is raised to $z^* = .625$. The "twin instabilities" are no longer found for any case, and phase speeds are found to be reduced. Changes in neither the inversion height nor its strength markedly modified the growth rate of the fastest growing mode. Figure 11 shows that the W^* tilt was greatly reduced by the low inversion, and when the inversion was strong, the structure of the vertical motion field no longer resembled that of the constant-lapse-rate case. From Figure 12 we see that the introduction of the higher

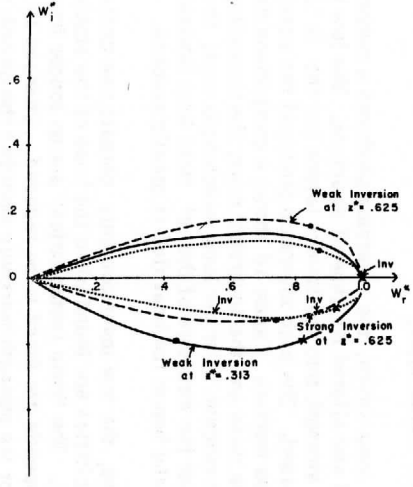

Figure 9. W^* hodograph, for constant shear case, $k^* = \ell^* = 1.0$, and temperature inversion bases at $z^* = .313, .625$. The inversion level is noted, and other features are the same as Figure 1a.

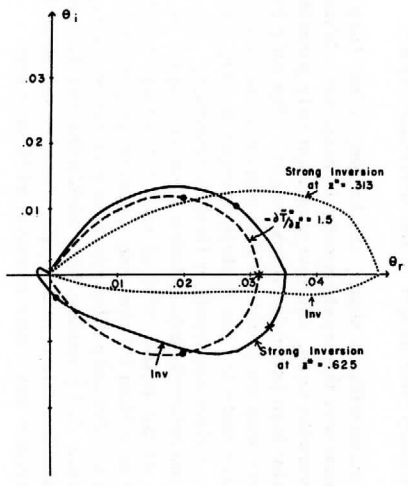

Figure 10. θ^* hodograph for constant shear case, $k^* = \ell^* = 1.0$, and temperature lapse rate, $-\partial\bar{T}^*/\partial z^* = 1.5$, or inversion bases at $z^* = .313, .625$. The inversion level is noted, and other features are the same as Figure 5.

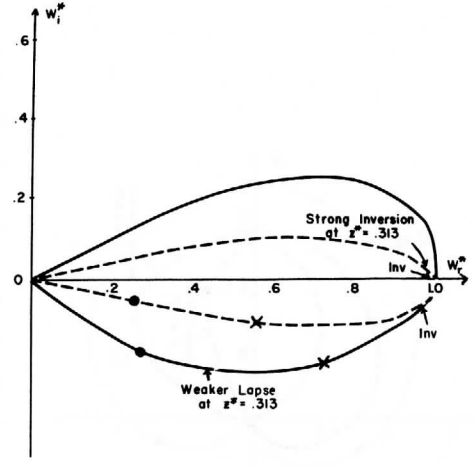

Figure 11. Same as Figure 9, except $k^* = \ell^* = 3.0$.

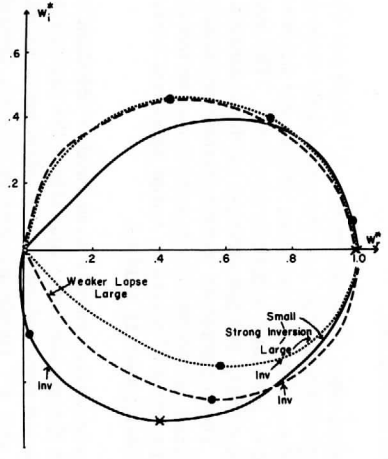

Figure 12. Same as Figure 11, except all inversion bases at $z^* = .625$. The relative growth rates are indicated.

inversion had only a minimal effect which occurred only in the upper layers; the point of $|W^*|$ maximum was at mid-level. Truncation is not observed in either case. The maximum vertical motion occurred at the top of the unstable layer when inversion is low.

The large changes that were produced in the θ^* field are shown in Figure 13. Tilts were greatly reduced, and the reductions were greatest for low, strong inversions. The low inversion profile did not even exhibit the shape characteristic of previous solutions any more. The maximum value was reduced in all cases, but the strength of the inversion was not the determining factor. The temperature perturbations very rapidly drop virtually to zero at the base of the inversion and remain so throughout the entire stable region. The point of maximum value appeared lower in the fluid than in the constant-lapse-rate studies.

The existence of an inversion in this case (with a constant wind shear present) greatly reduces the growth rates and alters the perturbation fields; the changes in structure are more noticeable for short wavelength modes. Here, as both the W^* and θ^* fields are greatly altered, though not in the same way, the heat flux is greatly reduced. In this way, the presence of stable regions is at least as important as the existence of a constant wind shear in modifying the convective instability.

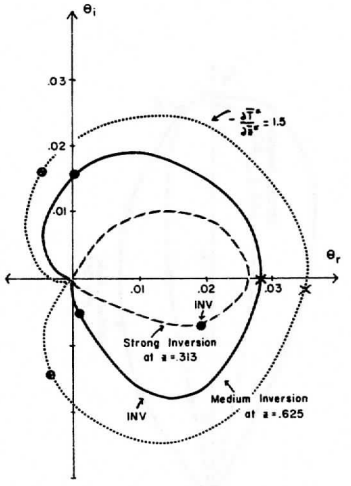

Figure 13. Same as Figure 10, except $k^* = \ell^* = 3.0$.

7. Turning of Wind with Height

We next examine changes which occur when the distribution of wind shear is no longer constant in magnitude and direction. Figure 14 shows the wind direction used: $\bar{U}(z)$ is the same as before, and $\bar{V}(z)$ increases linearly to mid-level, then decreases back to zero thereafter. It should be noted that $\partial\bar{V}^*/\partial z^*$ is negative in the upper half of the fluid although $|\partial\bar{V}^*/\partial z^*|$ is constant. All cases studied will again be for $k^* = \ell^*$. The magnitude of the total wind shear is now 14% greater than the constant-shear case.

In none of the studies with a variable vertical wind shear do we find the dual, mirror-image instabilities which are characteristic of the constant-shear, constant-lapse-rate, short wavelength regime. Considering these results, and those found by including variable temperature profiles (Section 6), we may conclude that the dual unstable modes are characteristic only of constant-shear, constant-lapse-rate environments.

First we will discuss variable shear with a uniform thermal stratification. From Table 1, we see that the growth rates are all enhanced relative to the constant-shear case, with the most significant changes occurring

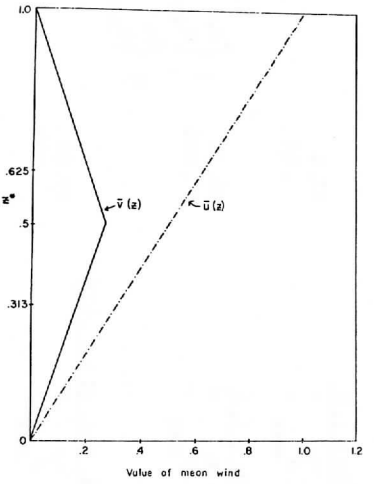

Figure 14. The wind distribution for the case when the wind turns with height.

Table 1*

	Wind turns with height		Const. shear	
	$k = \ell = 1.0$	$k = \ell = 3.0$	$k = \ell = 1.0$	$k = \ell = 3.0$
$\partial\bar{T}/\partial z = 0.33$				
σ_r =	14.39	7.116	5.91	nothing
θ_{max} =	.017	.0146	.0199	
$\partial\bar{T}/\partial z = 1.0$				
σ_r =	33.8	46.90	22.2	2: 7.54
θ_{max} =	.03	.0177	.027	modes .0348
$\partial\bar{T}/\partial z = 1.5$				
σ_r =	46.35	I σ_r = 67.42	30.8	2: 20.41
θ_{max} =	.036	I θ_{max} = .0198	.031	modes
		II σ_r = 3.04		
		II θ_{max} = .05		
Med. Inv. at z = .625				
σ_r =	39.83	50.24	38.3	I σ_r = 34.28
θ_{max} =	.033	.023	.035	I θ_{max} = .028
				II σ_r = 18.25
				II θ_{max} = .036
Med. Inv. at z = .313				
σ_r =	15.38	20.1	19.5	40.03
θ_{max} =	.053	.033	.044	.026

*All quantities are nondimensional.

for the long wavelength modes. θ^* maxima are not changed greatly when $k^* = \ell^* = 1.0$, but when the wavenumber becomes large, the temperature perturbations become weaker. The W^* profile appears slightly flattened, and its tilt is decreased. The θ^* profile has a much smaller tilt, and it more closely resembles the structure obtained when an inversion is present, rather than the constant-lapse-rate case. Although the growth rates of the instabilities are increased, the heat flux is smaller than was found with a constant shear. It is now apparent that though a variable shear profile affects the structure of the perturbations when wind and temperature fields are varied independently, the instabilities respond much more readily to the basic thermal field.

The next cases studied were those involving the inversion profiles introduced in the last chapter, and the shear profile of Figure 14. Table 1 shows that the variable shear produces some damping, and its effect is greatest for the short wavelength, low inversion combination. One one unstable mode was found in all cases. Figure 15 indicates that the inversion base at $z^* = .625$ has a minimal effect on W^* structure, though the lower inversion greatly reduces its tilt. All experiments for $k^* = \ell^* = 1.0$ showed minimal W^* tilt, so a hodograph would not prove fruitful. From Figure 16 we see that once again the high inversion produced a marked truncation in the θ^* field at the level of inversion. The low-level inversion greatly distorts the temperature perturbation field, and consequently any heat flux process would be severely hampered. The short wavelength modes, as shown in Figure 17, react more predictably to the existence of the inversion. The increased θ^* maxima, and sharp truncation at the inversion level are the same changes produced as the case when the wind shear was constant.

The observed differences seem to be related to the increase in the magnitude (by 14%) of the shear rather than the distribution of it. If the original constant shear $\bar{U}(z)$ had been transformed into a two-dimensional constant shear profile such that $\bar{U}(z) = \bar{V}(z)$ (and thus increasing the strength of the wind shear by 41%), no instabilities were found for any of the temperature distributions studied (see Figure 8). Asai found similar results. In addition, the turning of the wind did not greatly alter the effects of varying thermal stratification, which emerges as the key to the problem.

8. Basic Wind and Temperature Fields Related

All of the cases studied so far were designed to isolate the influence that changes in the shear and velocity profiles would independently have on low-level convection. None of them was taken as a possible representative condition in the real atmosphere (with the exception of the crude

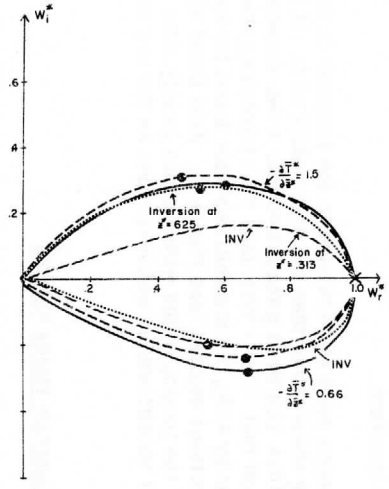

Figure 15. W^* hodograph for case where wind turns with height, $k^* = \ell^* = 3.0$; $-\partial \bar{T}^*/\partial z^* = 0.66$, 1.5, or inversion base at $z^* = .313$, .625. Other features are the same as Figure 9.

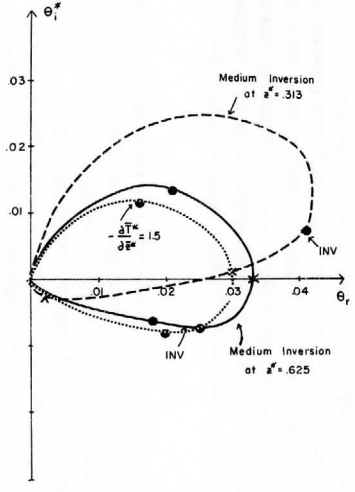

Figure 16. Same as Figure 10, except for case where wind turns with height.

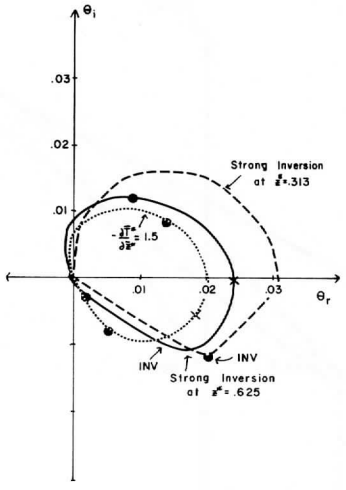

Figure 17. Same as Figure 16, except $k^* = \ell^* = 3.0$.

approximation to the Ekman spiral considered in the last section). It is usually found that in the real atmosphere, strong wind shear is present in thermally unstable regions. We may refer to this as the "realistic wind profile," which is a qualitative idealization not based on any real wind or temperature data. Figures 18a and 18b show the other shear profiles used. All are based on the above premise but some have no shear in the lower layer and increased shear in the upper layer to see whether the actual shear distribution produced any noticeable changes. In all cases the shear is unidirectional so that $\bar{V}^*(z) = 0$, and the shear $\partial \bar{U}^*/\partial z^*$ is always positive. All cases are for $k^* = \ell^*$, and the temperature profiles used are those of Figure 8.

From Figure 19, we see that, at the lower inversion height, the shear distribution did not greatly modify any of the growth rates for the long-wave case. With the higher inversion base, the strength of the shear in the lower, unstable region determines the amount the growth rates will be damped. Comparing these results to those obtained when constant-lapse rates were used indicates that the inclusion of inversions counters the damping effect of vertical wind shear.

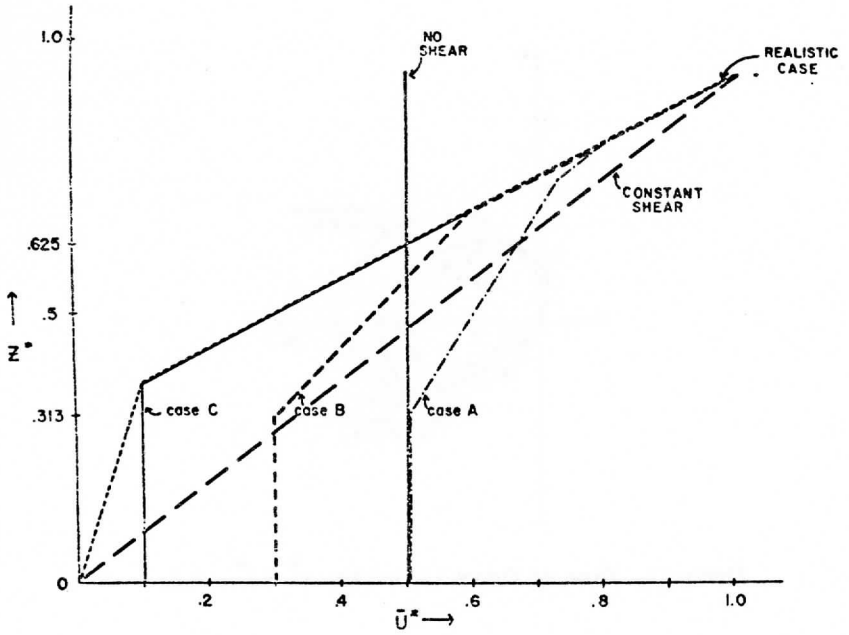

Figure 18a. Shear distribution used for inversion at $z^* = .313$.

All of the long wavelength modes found for the low inversion base showed a very small W^* tilt. Figure 20 shows a hodograph for Case A, which had the largest tilt and the weakest shear. (All figures are for strong inversion cases unless otherwise noted.) The points of maximum temperature and wind perturbations were not changed by varying the shear distribution. The θ^* phase was nearly constant, and as before, the perturbation field was concentrated in a small region just below the inversion base (Figure 21). The maximum θ^* value increased as the shear in the lower layers decreased.

When the inversion base was lifted to $z^* = .625$, the most noticeable effect was the elimination of the slower growing modes as the shear increased. The other changes produced by varying the inversion height were no different than those found when the wind shear was constant. Once again, changes in the inversion strength were not reflected in the profiles or the growth rates.

Introduction of a surface inversion beneath a thermally unstable region extending from $z^* = .313$ to the top of the fluid caused the model to behave as though it were turned upside down, i.e., the eigenvalues were nearly unchanged and the eigenvectors were mirror images about the mid-level. No other visible differences were found.

Changes in the shear distribution were more closely reflected in some of the characteristics of the short wavelength modes. When the inversion base was at point 5, the constant-shear profile, with a strong shear in the thermally unstable region, was by far the most efficient at damping growth rates. This again was more visibly true for the higher inversion level, as is shown in Figure 19. The strength of the shear in the unstable layer apparently holds the key to the growth rates of the unstable

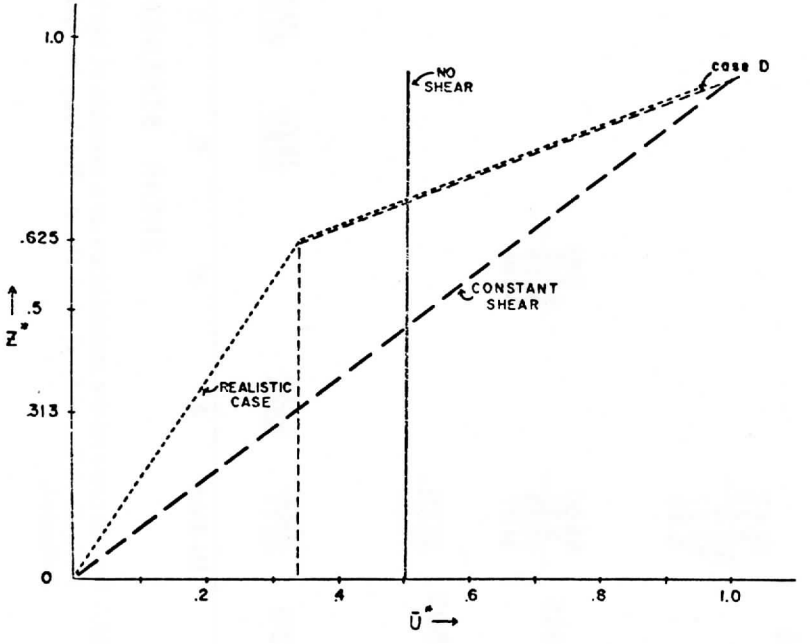

Figure 18b. Shear distribution used for inversion at $z^* = .625$.

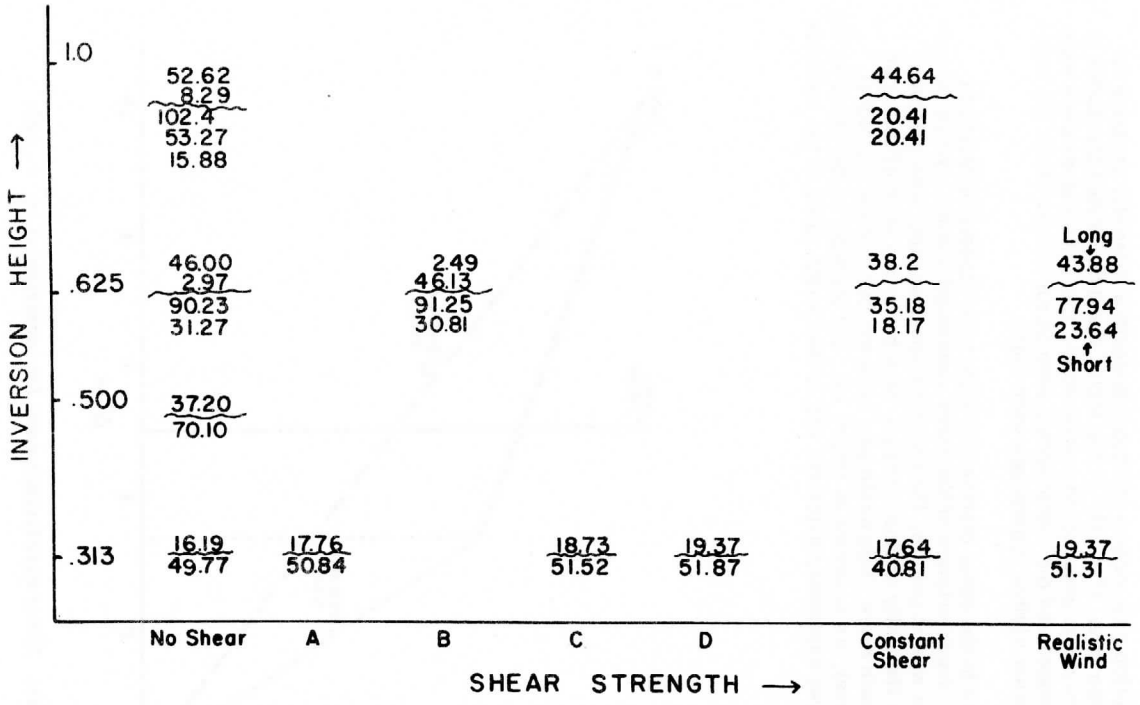

Figure 19. Growth rates of the instabilities as a function of the height of the inversion base and the strength of the vertical wind shear. The long wavelength and short wavelength modes are indicated.

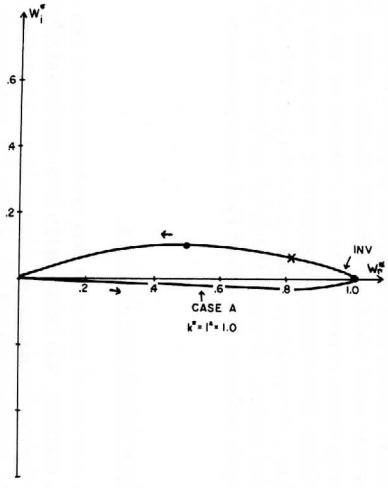

Figure 20. Same as Figure 9 for the Case A wind shear distribution and $k^* = \ell^* = 1.0$.

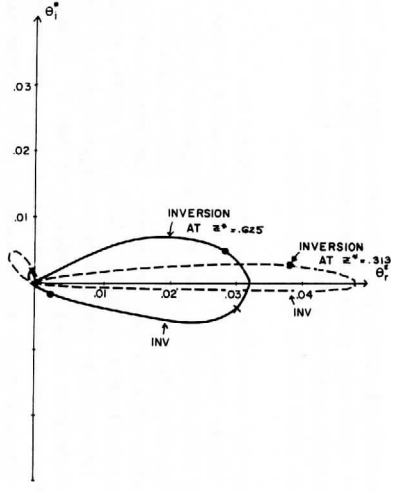

Figure 21. Same as Figure 10 except for the "realistic" wind shear case and $k^* = \ell^* = 1.0$.

modes; the two unstable modes grew at the same rate for the zero shear case and case A, despite the presence of a strong wind shear in the upper, stable layers.

As with the long wavelength cases for a low inversion base, the amount of tilt of the W^* field was inversely related to the average shear strength; the tilts were quite small in all cases. No other parameter reacted strongly to changes in the shear distribution.

Figure 22 shows that the low inversion base reduced the W^* tilt much more than did the higher inversion base. In all cases for the realistic wind, independent of wavelength, the W^* phase was nearly constant and more symmetric about the mid-level than when a constant shear was present. No truncation effects were present. The temperature perturbation field was also completely changed. All of the modes examined (see Figures 21 and 23) showed few distinct changes produced at the inversion level, and certainly no strong truncation of the θ^* field, as was found when the shear was constant. The tilts in all cases were greatly decreased, and the hodograph shape was not of characteristic form. For the short wavelength case, all $|\theta^*|$ maxima were greatly reduced, and the effects of the inversion were not as pronounced as in the previous cases. The heat flux was markedly reduced by the realistic wind profile due to the great changes in the temperature perturbation field.

In all the above cases, it was the variation in shear distribution which was important insofar as it represented a departure from the constant-shear profile. The perturbation temperature field was greatly reduced by reducing the shear strength in the lower unstable regions; although in the atmosphere the wind shear is usually weaker where thermal instability is high, it is in these regions that the strength of the shear is most important. In addition, the changes produced by variations in the thermal stratification (i.e., inversions) were markedly lessened by reductions in the mean wind shear. Hence, the joint action of the basic wind and temperature fields reduces the effect that each parameter has individually.

9. Wavelength and Wave Orientation Regimes

Up to this point, all of the discussion has centered about the case where $k^* = \ell^*$. In this section, we investigate how the instabilities are affected by changes in their orientation relative to the unidirectional mean flow by considering both quasi-longitudinal ($k^* << \ell^*$) and quasi-transverse ($\ell^* << k^*$) cases. The shear distributions will be those of the realistic cases of Figures 18a and 18b, and only strong thermal inversions

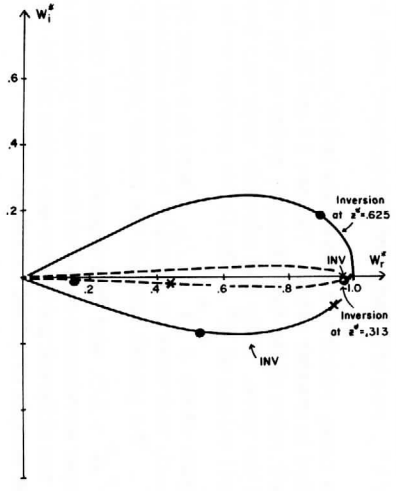

Figure 22. Same as Figure 9 except for the "realistic" wind shear case and $k^* = \ell^* = 3.0$.

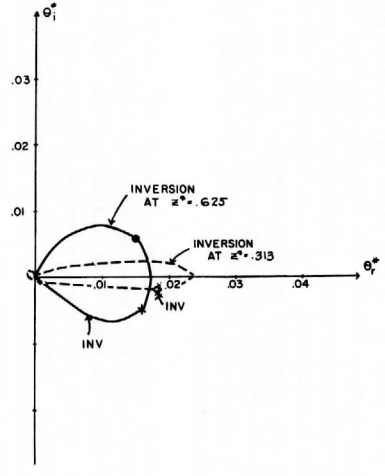

Figure 23. Same as Figure 21 except $k^* = \ell^* = 3.0$.

will be considered. We begin by examining what, if any, effect the realistic shear distribution has on the long and short wavelength regimes which were described earlier. When discussing these wavelength regimes, we will consider only $k^* = \ell^*$.

When the inversion base is at $z^* = .313$ there was no obvious distinction between the long and short wavelength regimes like that which appeared for the constant wind shear case. The region studied was $1.697 \leq K^* \leq 2.26$. As the wavenumber (K^*) was increased, the growth rates increased with only one unstable mode appearing. The $|\theta^*|$ maximum decreased slowly as the wavelength decreased, and the only structural change was a very slight increase in W^* tilt. The general form of the perturbation fields did not change.

A second, much weaker, instability appeared when $K^* = 1.697$. Its characteristics were totally dissimilar from those of the faster growth mode (it had a very large tilt); therefore no indication of the "twin" unstable modes was found. As the wavenumber was increased, the growth rates of both modes increased. The larger mode at the higher inversion grew twice as rapidly as the lower inversion mode. As with the lower inversion height, temperature perturbation maxima decreased slowly, but only minimal structural changes were observed as K^* increased. Phase speeds remained relatively constant.

Figure 24 shows clearly that varying the orientation of the wave did not result in any significant changes in the structure of the vertical wind perturbations. (In these experiments, K^* is held at the constant value 4.2 so that only the orientation is changed and the case $k^* = \ell^* = 3.0$ can be used as a reference point.) Growth rates and other parameters were found to be remarkably constant in these cases. Only the trace speed in the x-direction, $-\sigma_i^*/k^*$, was affected, and it increased with k^*.

The high-inversion case, which had previously led to more interesting results, was next studied in greater detail. Figures 25 and 26 show the dependence of the growth rates of the two unstable modes on the orientation and wavelength of the wave. Only one unstable mode was found in a limited region for small values of K^*. The faster growing mode shows a preference for the region where $k^*/\ell^* = 2/3$. There is a great dependence on ℓ^* when k^* is small, and there is possibly a second mechanism acting for small values of K^*. The growth rates of the slower growing mode prefer the region where $k^*/\ell^* = 3/2$, and that dependence more closely resembles that of the longer wavelength cases of the faster growing mode. It is very obvious that two different processes are acting on the two different modes. Phase speeds remained constant.

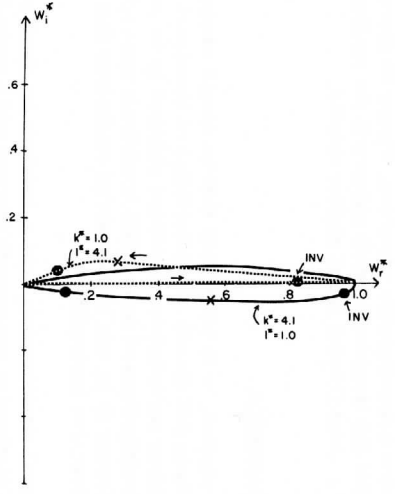

Figure 24. Same as Figure 22 except that inversion base is at $z^* = .313$; $k^* = 1.0$, $\ell^* = 4.1$, and $k^* = 4.1$, $\ell^* = 1.0$.

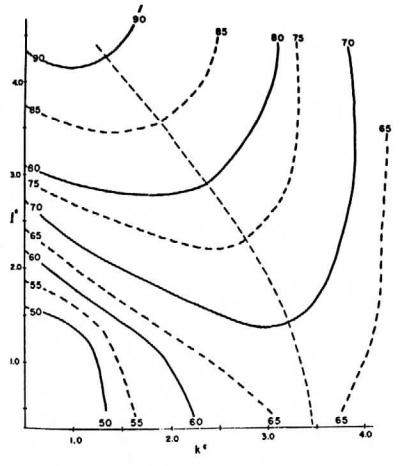

Figure 25. The growth rates for the fastest growing mode when the inversion base is at $z^* = .625$.

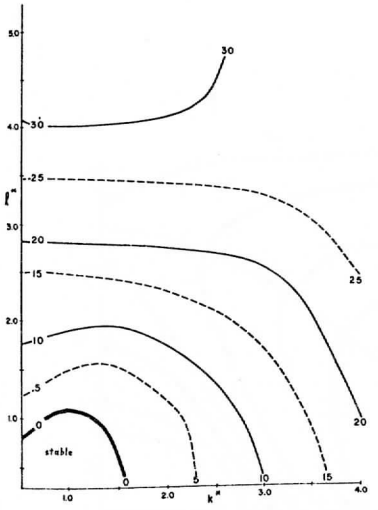

Figure 26. The growth rates of the slowest growing mode when the inversion base is at $z^* = .625$.

From Figure 27 we see that the tilts of the transverse ($k^* > \ell^*$) modes were much greater, and they more closely resembled the case where $k^* = \ell^* = 3.0$. The general structures were not greatly affected, and truncation effects were not noticeable anywhere. Figure 28 shows the θ^* hodographs; again the transverse mode appears to be similar to the case where $k^* = \ell^*$. Asai (1969a) found similar results.

10. Conclusions and Discussion

From all the cases studied, it is very clear that no single mechanism can determine the structural and growth characteristics of low-level convective instabilities. Many perturbation properties changed in an independent fashion when combinations of base-state conditions were tried, and thus there did not appear to be any simple set of conditions that would most enhance convective instabilities.

When constant thermal stratification, and a constant (or zero) wind shear was present, two distinctive wavelength regimes and a clear transition region were found. Growth rates were dependent upon the wavelength, and were larger when the constant wind shear was removed. Further

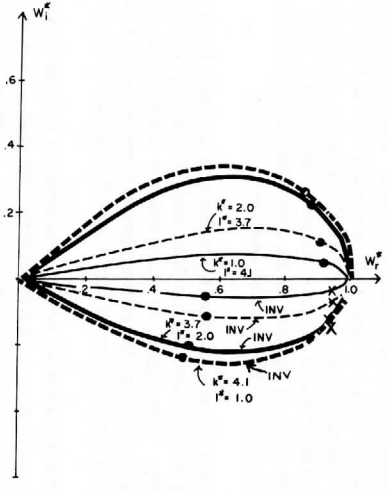

Figure 27. Same as Figure 22 except the inversion base is at $z^* = .625$. The wavenumbers are indicated.

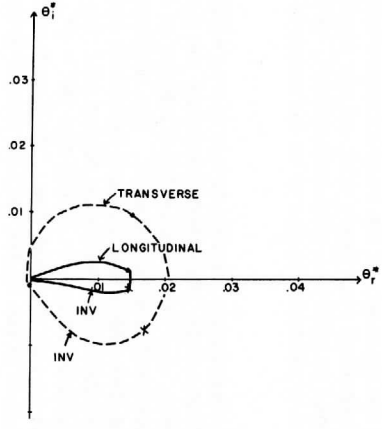

Figure 28. Same as Figure 21 except the inversion base is at $z^* = .625$, and it is for the transverse and longitudinal modes.

examinations led us to conclude that these two regimes are characteristic of the special class of conditions stated above, and hence no generalizations can be made using those results.

Growth rates and the intensity of the temperature perturbations were found to be strongly dependent upon lapse rate, as one would expect. No other significant changes in structure were encountered, and it was concluded that the thermal dependence seems to be far stronger than the wind-shear dependence.

The existence of temperature inversions has strong effects on convective processes. First of all, they tend to obscure the damping caused by a constant wind shear, and hence make the existence of a constant wind shear a less important factor to consider. The temperature perturbation field was concentrated into a small region below the stable layer, and it was sharply truncated once the stable region was reached. The W^* field was not so greatly affected. Hence the $W^* - \theta^*$ correlation was reduced, and thus so was the heat flux. The height of the inversion base, and not the strength of the stable region, proved to be the crucial parameter.

The instabilities showed a preference for the longitudinal modes rather than the transverse ones and that preference was strongly evident in their comparative growth rates. This preference was not entirely the rule and could be decreased by altering the wind and temperature structure.

When the wind and temperature fields were related in a qualitatively realistic way, the greatest changes were the reduction of the tilt of the W^* and θ^* fields. A constant shear was very efficient in damping growth rates for constant lapse rate environments. The strength and distribution of the wind shear did not prove to be important in the thermally stable regions (where the wind shear is normally strong), but its magnitude was very significant in the unstable regions (where the wind shear is normally weak). There did not appear to be any significant distinctive regimes based on wavelength for any of the realistic cases.

There also appeared to be a distinct preference in growth characteristics with certain wave orientations for the realistic wind, but these varied with wavelength. Two differing mechanisms seem to be causing the two unstable modes, and as the slower growth mode has a higher phase speed, a study of its characteristics could turn out to be fruitful.

We believe that future studies could concentrate on the explanation for the preference for certain wave orientations and this could possibly be traced back to the causes of the instabilities. More attention should be paid to the thermal structure, and its probable joint influence with the

wind shear, especially in the unstable regions. Finally, actual data could be supplied to test out whether this model holds any promise for understanding the real atmosphere and its processes.

Acknowledgments

The authors would like to thank Professor David D. Houghton for his many valuable suggestions and criticisms.

Financial support was provided by the Environmental Science Services Administration under grant number E-230-68-(G) at the Space Science and Engineering Center of the University of Wisconsin. Computing funds were provided by the Wisconsin Alumni Research Foundation at the University of Wisconsin Computing Center.

References

Asai, T. 1964. "Cumulus Convection in Atmosphere with Vertical Wind Shear: A Numerical Experiment," J. Meteor. Soc. Japan Series II, 42 (4), 245-259.

Asai, T. 1969. "Stability of a Plane Parallel Flow with Variable Vertical Shear and Unstable Stratification," NCAR Manuscript 69-194.

Asai, T. 1969a. "Three Dimensional Features of Thermal Convection in a Plane Couette Flow," NCAR Manuscript 69-99.

Faller, A. J. 1965. "Large Eddies in the Atmospheric Boundary Layer and their Possible Role in the Formation of Cloud Rows," J. Atmos. Sci., 22, 176-184.

Faller, A. J. and Kaylor, R. 1966. "A Numerical Study of the Instability of the Laminar Ekman Boundary Layer," J. Atmos. Sci., 23, 466-480.

Faller, A. J. and Kaylor, R. 1967. "Instability of the Ekman Spiral with Applications to the Ekman Boundary Layer," Physics of Fluids Suppl. — Boundary Layers and Turbulence, 10 (9), S212-S219

Ingersoll, A. P. 1966. "Convective Instabilities in Plane Couette Flow," Physics of Fluids, 9 (4), 682-689.

Ingersoll, A. P. 1966a. "Thermal Convection with Shear at High Rayleigh Number," J. Fluid Mech., 25, 209-216.

Jeffreys, H. 1928. "Some Cases of Instability in Fluid Motion," Proc. Royal Soc., A118, 195-208.

Lilly, D. K. 1966. "On the Instability of Ekman Boundary Flow," J. Atmos. Sci., 23, 481-494.

Pellew, A. and Southwell. 1940. "On Maintained Convective Motions in a Fluid Heated from Below," Proc. of the Royal Soc. Series A, 176, 312-343.

Rayleigh, Lord. 1916. "On Convective Currents in a Horizontal Layer of Fluid when the Higher Temperature is on the Under Side," Phil. Mag., 32, 529-546.

Schlichting, H. 1968. Boundary Layer Theory, McGraw-Hill.

Stommel. 1948. "Summary of the Theory of Convection Cells," Proc. N. Y. Acad. of Sciences.

Near Real Time Rectification and Gridding of Apt Satellite Pictures

John Thomas Young, Jr.

Abstract

A technique is described in which an ordinary APT satellite picture is received and at least three geographic features identified. The satellite signal is digitized in real time by the Raytheon 440 computer. The picture coordinates and earth coordinates of the geographic features are used to generate a new format (polar stereographic projection) and grid the picture via a computer program. A new picture, having the full resolution and dynamic range of the original, is available about thirty-five minutes after receipt of the satellite picture. The new picture is reproduced on a facsimile with signals having characteristics identical to ordinary facsimile signals and could be relayed to many weather stations.

Introduction

This research was undertaken to determine the feasibility of gridding and rectifying APT (automatic picture transmitting) satellite pictures based on geographic reference points found in the pictures. It was anticipated that this technique coupled with rectification of the picture to a standard meteorological map projection would vastly improve the utility of these real-time pictures for both research and operational analysis and forecasting use. In either digital or pictorial format the cloud information in the picture could be compared directly with conventional meteorological data.

The APT satellites are near-polar orbiting, sun-synchronous satellites producing slow scan, earth-oriented pictures. The NOAA-8 satellite used in this experiment produces a picture of an area 1700 n. mi. wide from an altitude of 750 n. mi. Figure 1 shows the relationship between the satellite picture and the satellite orbit. The shutter on NOAA-8's vidicon camera system is released when the camera is directed toward the subsatellite point. The image is formed by a wide-angle lens on the vidicon screen from which it is immediately scanned and transmitted to any appropriately equipped

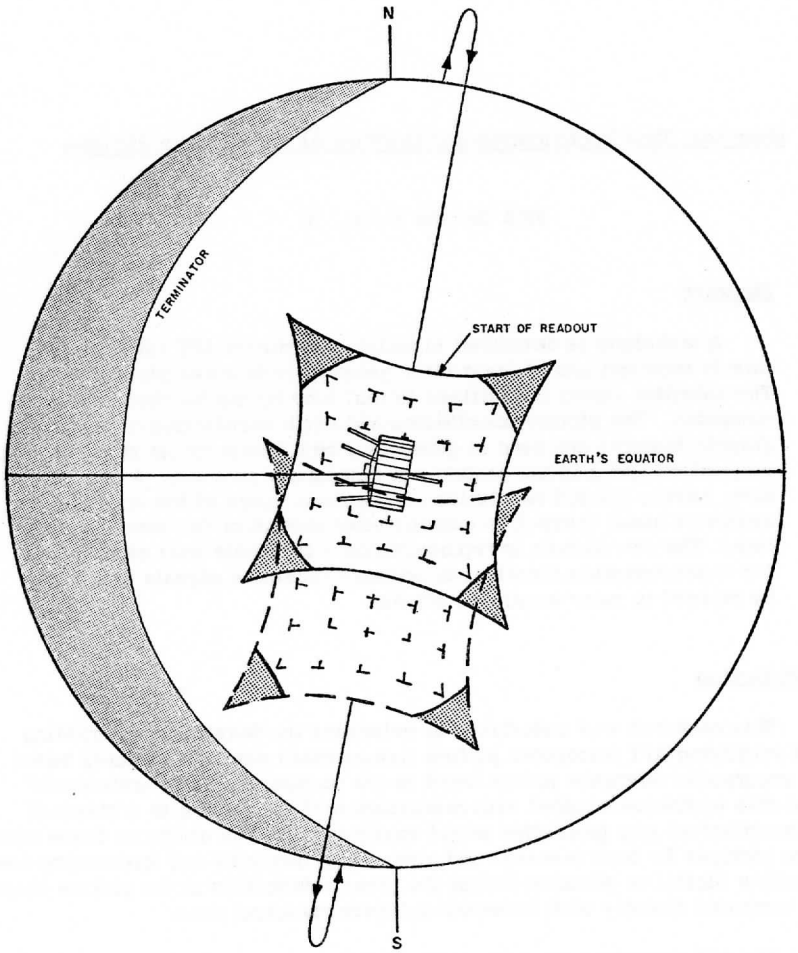

Figure 1. The satellite picture and orbit relationship

ground station. The picture transmission time is 200 seconds at a scan rate of four lines per second. The video data scanned from the vidicon is used to amplitude modulate a 2400 HZ signal which frequency modulates the 137.62 MHZ carrier frequency. An eight-picture sequence is transmitted each orbit with the interval between pictures set to provide a 30% overlap between consecutive pictures.

Statement of Problems

The conventional manual gridding technique as described in the "ESSA Direct Transmission Users Guide" [1] involves projecting a grid onto the picture and tracing the latitude and longitude lines onto it. After the picture is received, the subsatellite point and, nominally, the picture's principal point are determined from the observed picture time and ephemeris data for that orbit. The appropriate grid, recorded on 35 mm. film, is selected based on the latitude of the subsatellite point. This grid is projected onto the picture so that the subsatellite point is properly positioned. Then the picture is rotated to align the heading line, represented by the north-south center fiducials, to be parallel with the north-south reference marks on the grid. When geographic reference points are visible in the picture, the grid should be aligned to them. It may be necessary to adjust the projected grid size and to rotate and translate the picture to obtain a good fit before tracing the grid onto the picture. Actually, the grid for a picture is unique to the satellite's attitude and subpoint, thus an infinite number of grids should be available. Such a procedure is usually iterative and frequently requires ten to fifteen minutes to complete.

Two types of systematic distortion are found in the pictures. The first is projection distortion of the earth's latitude and longitude grid caused by the projection of the earth sphere onto a plane surface. The result is a foreshortening of the grid toward the edges of the picture with a subsequent reduction of one-third in earth surface resolution from subsatellite point to outer edge of the picture. Also the grids in the overlap area of two pictures cannot be aligned, and therefore, information in this area of the two pictures cannot be compared directly, as with a stereo viewer, for example. Thirdly, the data are in a projection quite different from the projections used to display conventional data, making direct comparisons difficult.

The second type of distortion is due to a combination of camera lens, vidicon scan, and facsimile distortions. RCA's Astro Electronics Division, producers of the NOAA-8 satellite, measured this combination of distortions during prelaunch calibration tests by analyzing a Mufax picture of a test target. The results are presented in a report under contract NAS 5-9034 in the form of a graph of look angle versus facsimile print distance from the center. This distortion, which is peculiar to each satellite, cannot be

corrected in the general purpose 35 mm. grids; therefore, the use of the grids in manual gridding produces an inaccuracy of as much as 10 n. mi. in some portions of the picture.

Any attempt to grid APT satellite pictures accurately, using geographic features, must take the above mentioned factors into account. In addition, the processing time required to grid and remap a picture should not significantly exceed the manual gridding time. The final projection chosen for the picture should be compatible with one of the standard meteorological map projections used to display conventional data. The scale of the projection must also be close to the original picture scale so that information is not lost due to compression or large gaps produced by expansion. Fortunately, a 1:20,000,000 scale polar stereographic projection fulfills these conditions for hi- and mid-latitude pictures, and is used in the NMC 850 mb. and 500 mb. analyses for facsimile transmissions.

Approach to the Problem

To perform the corrections discussed above, it is necessary to rearrange the geometry of the data in the picture to accomplish the change in projection. Since rectification and gridding are based on geographic features in the picture, the real-time picture must be reproduced and analyzed. Thus, the gridding cannot be performed in real time. Computer processing is a logical choice since all corrections can be made in one pass through the data. The signal can be digitized in real time as a picture is being produced. The picture coordinates and earth coordinates for three points in the picture are required for input to the computer program. After processing the new picture is reproduced on a facsimile machine. In the computer program written for the UNIVAC 1108, the coordinates of the three points are used to find a best-fit subsatellite point and satellite altitude. Using this information and the look angle for each data element, as determined from the RCA calibration curve, the elements are repositioned into the polar stereographic projection. If an element is located on a 5° latitude or longitude line, it is set to a white brightness value, thus producing the grid lines. Since it is necessary to expand the picture slightly to achieve the 1:20,000,000 scale, data gaps which occur must be averaged out using the brightness values of their neighbors.

Procedure

Throughout the experiment typical APT ground station equipment and standard procedures are used [1], [2]. Therefore, only the equipment and procedures developed for this experiment will be detailed. A typical ground station consists of a steerable antenna to acquire and track the satellite, a

receiver to amplify and demodulate the FM signal, and a facsimile recorder to produce the picture. To format the data for computer processing, it is necessary to convert the video signal from analog to digital signal. The hardware necessary to do that is shown in Figure 2. The video signal from the receiver is separated from the 2400 HZ subcarrier with a synchronous detector and sent to the Raytheon 440's analog-to-digital converter. The sampling of the video is controlled by a 4800 HZ pulse train derived from the subcarrier of the satellite. Sampling at 4800 HZ is required to preserve the video bandwidth of 1600 HZ. The pulse train goes to the computer's external interrupt. The computer samples the video signal once for each pulse received and stores the digital brightness in core. Six bit samples are used to maintain the dynamic range of the signal. After 1200 elements (one scan line) are accumulated in memory, the line is transferred to magnetic tape.

Immediately after the end of the picture transmission, the real-time APT picture must be examined for geographic reference points. A nonlinear transfer function is used in the facsimile machine to make the lower signal level geographic features more prominent. Three reference points are chosen as far from the picture center as possible. The latitude and longitude of these points are obtained from a detailed map of the area. The picture coordinates of these points are measured using the center as origin with positive Y-axis perpendicular to the scan line toward top (first scan line) of the picture, as shown in Figure 3. The X-axis is along the center scan line toward the right parallel to the scan lines. The picture coordinates are given in inches from the center with measurements made to 0.01 inches. 0.01 inches corresponds to one scan line. The reference point coordinates are punched on computer cards for input to the program and processed on the UNIVAC 1108 computer.

To reproduce the processed picture, the Raytheon 440 computer is connected to the photo-facsimile machine through a digital-to-analog converter and a low pass filter and remodulation circuit. The data are clocked out of the computer with 4800 HZ pulse train derived in this case from a crystal oscillator. All frequencies in the video above 1600 HZ are filtered out, and a 2400 HZ carrier, also obtained from the crystal oscillator, is AM modulated by the video data. This signal goes to the facsimile recorder to produce the new picture.

Computer Program

A flow chart of the program is presented in Figure 4. In the program a subroutine developed and proven in ATS satellite picture navigation schemes obtains the subsatellite point and satellite altitude by least squares fit. Two matrices are then set up, one for the original data and the other for

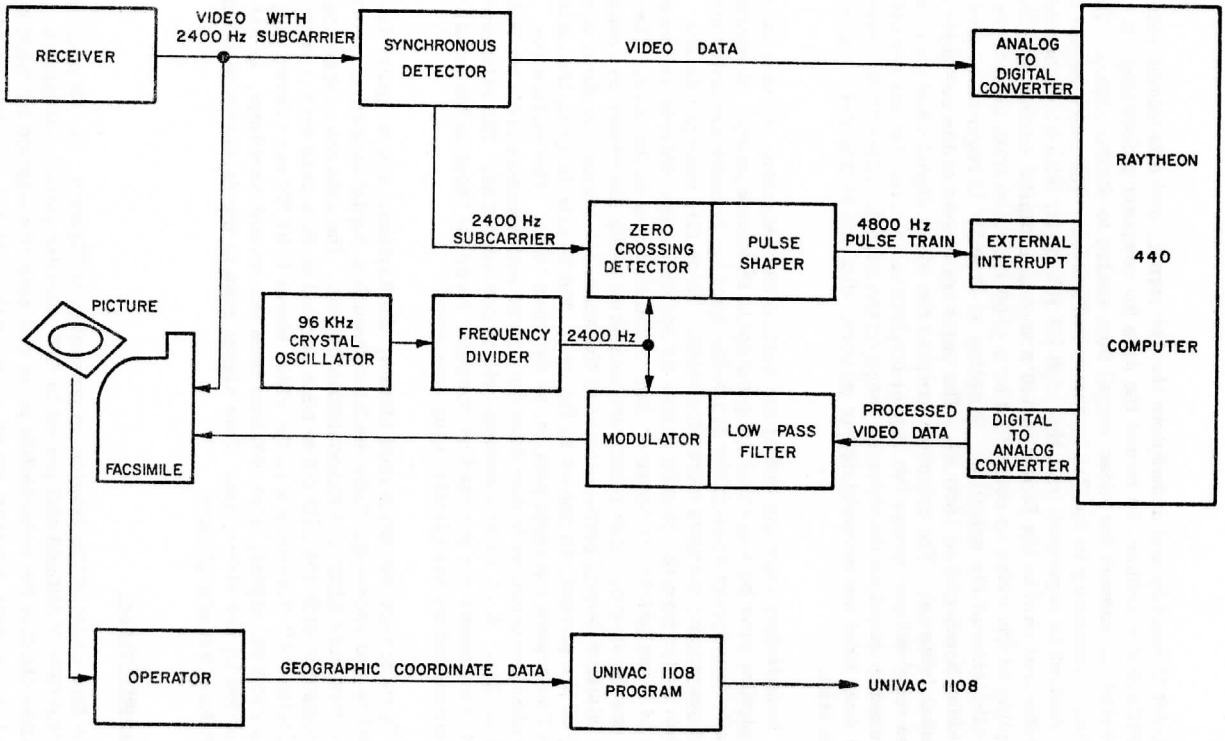

Figure 2. A block diagram of the equipment

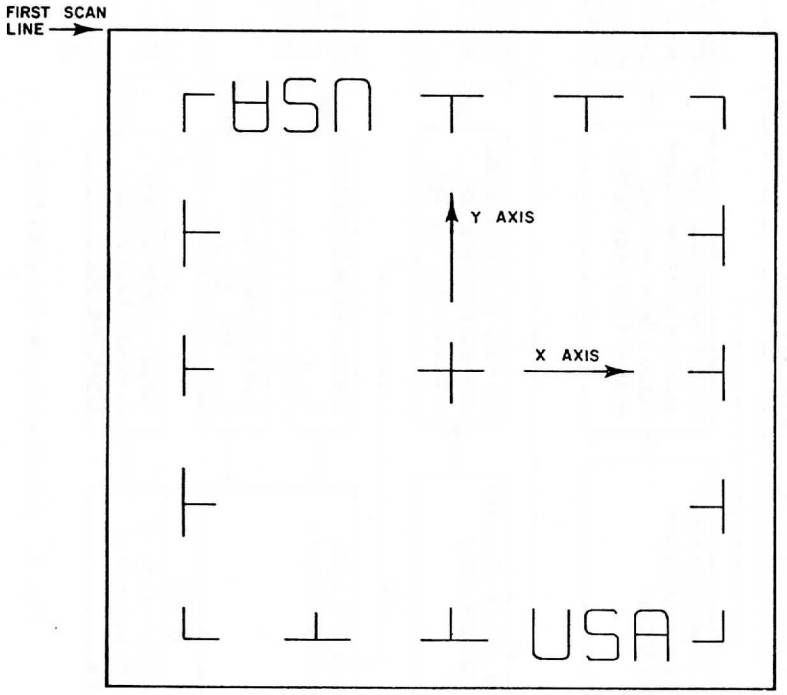

Figure 3. Picture scan format with picture coordinates added

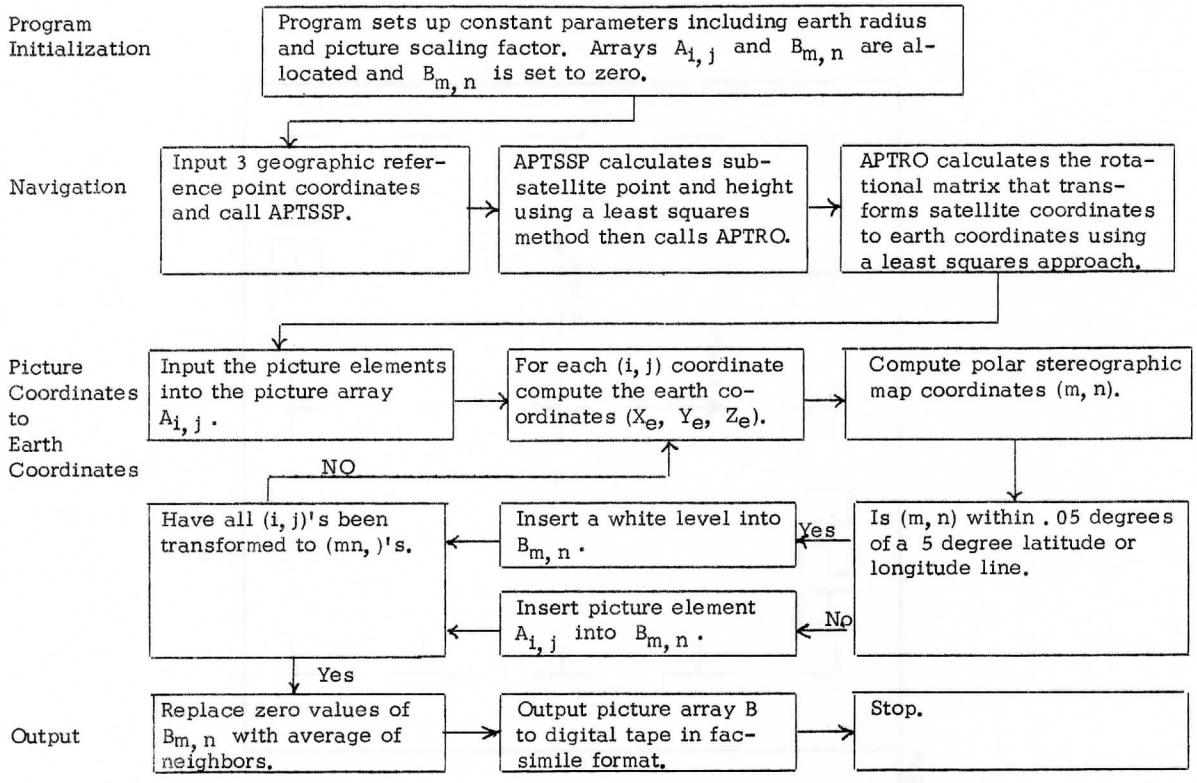

Fig. 4. Flow Chart for the Computer Program

the transformed data. The positions of elements in the matrices correspond to their positions in the picture. The original data matrix is A_{ij}, where i is the element number from left to right in a scan line and j is the scan line number starting at the first line transmitted by the satellite. The picture coordinates of a point are obtained by:

$$X = i - 570$$

$$Y = 400 - j$$

The look angle (η) is found from

$$\eta = c_1\sqrt{X^2 + Y^2}(1 - c_2\sqrt{X^2 + Y^2}), \text{ where } c_1 = 0.15601$$

$$c_2 = 7.8874 \times 10^{-4}$$

c_1 and c_2 are obtained from a least squares fit to a parabolic equation of the RCA calibration curves previously mentioned. SVEC is a vector in satellite picture coordinates through a picture element to the earth's surface. The coordinates of a unit vector in the direction of SVEC are given by:

$$d = X/\sqrt{X^2 + Y^2} \sin(\eta)$$

$$e = Y/\sqrt{X^2 + Y^2} \sin(\eta)$$

$$f = -\cos(\eta)$$

where SVEC = g(d, e, f).

The magnitude (g) of SVEC is obtained from the equation for the intersection of this vector with earth's surface

$$(gd - a)^2 + (ge - b)^2 + (gf - c)^2 = R^2$$

R is the radius of the earth, and a, b, and c are found from the equation for the earth's surface

$$(X_e - a)^2 + (Y_e - b)^2 + (Z_e - c)^2 = R^2$$

X_e and Y_e are in the plane of the equation with X_e toward the prime meridian and Y_e toward 90° E. Z_e is along the earth's axis toward the north pole. g is the smallest root of the equation for the intersection.

EVEC is the position vector in the earth's coordinate system for the intersect of SVEC, with the earth's surface. It is the sum, in the earth's coordinates, of the satellite's position vector, ESAT, and SVEC in the earth coordinates. Thus

$$\underline{EVEC} = STOE\ \underline{SVEC} + \underline{ESAT}$$

STOE is the rotational matrix for satellite coordinates to earth coordinates transformation. STOE and ESAT are obtained from the subsatellite point and satellite altitude.

A polar stereographic map is the projection of the earth's surface onto a plane tangent to the surface at a pole. The radiance point is the opposite pole. The equations for conversion from earth coordinates to polar stereographic coordinates are:

$$X_p = K\, X_e/(Z_e + R)$$

$$Y_p = K\, Y_e(Z_e + R)$$

K is the scaling factor needed to obtain a 1:20,000,000 map. The center of the map coordinate system is translated to the satellite subpoint and rotated through the subpoint longitude angle to obtain the new picture coordinates (X_t, Y_t) with the subsatellite point in the picture center and north toward the top center

$$X_c = X_p - X_{p,s}$$

$$Y_c = Y_{p,s} - Y_p$$

$$X_t = Y_c \cdot \cos(\text{long}) + X_c \cdot \sin(\text{long})$$

$$Y_t = -Y_c \cdot \sin(\text{long}) + X_c \cdot \cos(\text{long})$$

$X_{p,s}$ and $Y_{p,s}$ are the coordinates of the subsatellite point in polar stereographic coordinates. In the second matrix $B_{m,n}$; $m = X_t$ and $n = Y_t$. Before each brightness value is transferred to $B_{m,n}$ from $A_{i,j}$ the latitude and longitude of the element is calculated. If the latitude or longitude is within .05 degrees of a 5° line, the brightness value for white is placed in $B_{m,n}$ rather than the original brightness value. Otherwise, the brightness value in $A_{i,j}$ is transferred to $B_{m,n}$.

Since the data in $B_{m,n}$ is expanded slightly, the data gaps must be averaged out. When $B_{m,n}$ was set up, it was initialized to zero brightness values. All zero values in $A_{i,j}$ are set to value one before transfer. Therefore, after all transfers are completed, any zero values represent data gaps. The matrix is searched for zero values, and they are replaced with the average values of the nearest nonzero neighbors. $B_{m,n}$ is finally transferred to magnetic tape for reproduction.

Results

On March 8, 1971, a picture was acquired from the NOAA-8 satellite at 16:15:53 GMT on orbit 10206. The approximate subsatellite point was 47.3° N., 85.5° W. This picture is shown in Figure 5. Three geographic reference points were chosen: the peninsula between Upper Red Lake and Lower Red Lake in Minnesota, the mouth of the Attawapiskat River on Hudson Bay, and snow-free Milwaukee, Wisconsin. The picture was then computer processed in the manner described above. The gridded and rectified picture is shown in Figure 6. Four geographic features other than the three reference points were chosen to check the gridding accuracy of the picture. The largest observed error was 0.1 degrees and the smallest error was 0.05 degrees.

Due to the lack of dimensional stability of the electrolytic facsimiles used to reproduce the NMC maps, the maps may vary slightly from the 1:20,000,000 scale. Thus, a perfect match will not always be possible. However, the processed picture does have a 1:20,000,000 scale.

The processing time from the ending of the real-time picture to ending of the processed picture was thirty-five minutes. The largest portion of this time (twenty-five minutes) was computer time. Because of the time sharing procedure used in the UNIVAC 1108 only fourteen minutes of the twenty-five were required actually to process the picture. Thus, a dedicated computer of equal speed would reduce the total processing time to twenty-four minutes.

It is, therefore, possible to rectify and grid APT satellite pictures in near real time based on geographic features in the picture. The product has a higher utility and is more versatile. For example, the characteristics of the signals used to reproduce the processed picture are the same as those used in ordinary weather facsimile transmissions; thus the new pictures could be relayed to other locations.

Moreover, the ATS satellite real-time pictures of the United States could be processed in the same manner described above and transmitted to weather stations so that a time sequence of pictures could be made available to local weather stations.

References

1. ESSA Direct Transmission System Users Guide, U. S. Dept. of Commerce, 1959.

2. Vermillion, C. H., Constructing Inexpensive Automatic Picture-Transmission Ground Stations, National Aeronautics and Space Administration, NASA SP 5079, 1968.

Figure 5. Original picture

Figure 6. Processed picture